Published in final edited form as:
Nat Mater. 2019 August ; 18(8): 892–904. doi:10.1038/s41563-019-0377-5.

Long-Term Implant Fibrosis Prevention in Rodents and Non-Human Primates Using Localized Deliverable Crystals

Shady Farah[1,2,3,*], **Joshua C. Doloff**[1,2,3,12,*], **Peter Müller**[4], **Atieh Sadraei**[1], **Hye Jung Han**[1,3], **Katy Olafson**[1,2,3,5], **Keval Vyas**[1], **Hok Hei Tam**[1,3], **Jennifer Hollister-Locke**[6], **Piotr S. Kowalski**[1,2], **Marissa Griffin**[1], **Ashley Meng**[1], **Malia McAvoy**[1,7], **Adam C. Graham**[8], **James McGarrigle**[9], **Jose Oberholzer**[9], **Gordon C. Weir**[6], **Dale L. Greiner**[10], **Robert Langer**[1,2,3,7,11], **Daniel G. Anderson**[1,2,3,7,11,#]

[1] David H Koch Institute for Integrative Cancer Research, Massachusetts Institute of Technology, 500 Main Street, Cambridge, Massachusetts 02139, USA.

[2] Department of Chemical Engineering, Massachusetts Institute of Technology, 77 Massachusetts Avenue, Cambridge, Massachusetts 02139, USA.

[3] Department of Anesthesiology, Boston Children's Hospital, Harvard Medical School, 300 Longwood Ave, Boston, Massachusetts 02115, USA.

[4] X-Ray Diffraction Facility, MIT Department of Chemistry, Massachusetts Institute of Technology, 77 Massachusetts Avenue, Cambridge, Massachusetts 02139, USA.

[5] Department of Chemical and Biomolecular Engineering, University of Houston, Houston, TX 77204

[6] Section on Islet Cell and Regenerative Biology, Research Division, Joslin Diabetes Center, One Joslin Place, Boston, MA 02215, USA.

[7] Harvard-MIT Division of Health Science Technology, Massachusetts Institute of Technology, 77 Massachusetts Avenue, Cambridge, MA, 02139, USA

[8] Center for Nanoscale Systems, Harvard University, Cambridge, MA, USA.

[#] dgander@mit.edu; Tel.: +1 617 258 6843; fax: + 617 258 8827.

[*] Equal contributing authors.

AUTHOR CONTRIBUTIONS

S.F., J.C.D., and D.A. designed the studies, analysed data, and wrote the paper. S.F., J.C.D., P.M., A.S., H.J.H., K.O., K.V., H.H.T., J.H-L., P.S.K., M.G., A.M., M.M., A.C.G., J.M., and J.O. conducted the experiments. S.F. and J.C.D. carried out the statistical analyses and prepared displays communicating data sets. G.C.W. and D.L.G. provided advice and technical support throughout. R.L. and D.A. supervised the study. All authors discussed the results and the preparation of the paper.

COMPETING FINANCIAL INTERESTS

The authors have no competing financial interests to declare.

Ethical Compliance Statement

We confirm that we have complied with all relevant ethical regulations, as specified in further detail in the above animal methods section.

Data availability

Data supporting the findings of this study are available within the article [and its supplementary information files] and from the corresponding author upon reasonable request.

[9] Department of Surgery, Division of Transplantation, University of Illinois at Chicago, 840 S. Wood Street, Chicago, IL 60612, USA.

[10] Program in Molecular Medicine, University of Massachusetts Medical School, Worcester, MA 01605, USA

[11] Institute for Medical Engineering and Science, Massachusetts Institute of Technology, 77 Massachusetts Avenue, Cambridge, Massachusetts 02139, USA.

[12] Present address: Department of Biomedical & Materials Science Engineering, Translational Tissue Engineering Center, Wilmer Eye Institute & the Institute for NanoBioTechnology, Johns Hopkins University School of Medicine, Baltimore, MD 21231, USA.

Abstract

Implantable medical devices have revolutionized modern medicine. However, immune-mediated foreign body response (FBR) to the materials of these devices can limit their function or even induce failure. Here we describe long-term controlled release formulations for local anti-inflammatory release through the development of compact, solvent-free crystals. The compact lattice structure of these crystals allows for very slow, surface dissolution and high drug density. These formulations suppress FBR in both rodents and non-human primates for at least 1.3 years and 6 months, respectively. Formulations inhibited fibrosis across multiple implant sites—subcutaneous, intraperitoneal and intramuscular. In particular incorporation of GW2580, a Colony Stimulating Factor 1 Receptor (CSF1R) inhibitor, into a range of devices including human islet microencapsulation systems, electrode-based continuous glucose-sensing monitors and muscle-stimulating devices, inhibits fibrosis, thereby allowing for extended function. We believe that local, long-term controlled release with the crystal formulations described here enhances and extends function in a range of medical devices and provides a generalized solution to the local immune response to implanted biomaterials.

Implanted biomedical devices are an integral part of modern therapeutics, playing key roles in many clinical applications including neural interfacing[1], monitoring vital signs[2], pacemakers[3], controlled drug release[4], scaffolds for tissue reconstruction[5], vascular stenting, cell encapsulation and transplantation[6]. While the immunological response to materials can be therapeutic, for example with particulate vaccines[7], some device materials, including polysaccharides, polymers, ceramics, and metals[8], can induce host immune-mediated foreign body and rejection responses This response can lead to fibrotic encapsulation, and in some cases, reduced efficacy or failure[8–12]. Current approaches for long-term maintenance of biomedical device implant biocompatibility often involve broad-spectrum anti-inflammatories[13]. Short-term steroid or anti-fibrotic drug delivery can transiently inhibit inflammatory cell recruitment as well as improve protein secretion of immuno-isolated cellular grafts[14,15]. However, many anti-inflammatory drugs have multiple targets and differential effects *in vivo*, and associated toxicity[13,16]. In particular, macrophages are known to be key mediators of the immune response to implanted biomaterials[8–10]. Recently it was shown that the implant-induced foreign body response can be inhibited through selective targeting of the monocyte/macrophage-expressed colony stimulating factor-1 (CSF1R) receptor[10]. Importantly, while macrophage numbers in the IP space as well as other essential macrophage functions, such as VEGF production, wound healing, and phagocytosis, were found to be left intact[10], cellular phenotype was different both at the level of RNA (gene expression) and protein (FACS), indicating a shift in macrophage behavior. Inhibition of CSF1R has also previously been shown to induce macrophage polarization[17].

Systemic application of broad-spectrum non-steroidal anti-inflammatories have been associated with hepatocellular, cardiac, or renal toxicities[18], gastrointestinal ulceration bleeding and microbial dysbiosis[19]. Specific inhibitors of molecular targets implicated in macrophage response can have side effects when dosed globally. For example, TNFα inhibitors can increase infection occurrence and risks of autoimmunity, and worsen neurologic and/or congestive heart failure prognosis[20]. Anti-TGFβ compounds can increase risks of autoimmunity and cancer (keratoacanthomas)[21], and those against CSF1R receptor can elicit fatigue/asthenia, edema and assorted other side effects[17]. Given that there are macrophage populations in every major tissue of the body[22], we sought to develop a long-lasting, localized delivery system. Locally releasing, drug-eluting devices have demonstrated their utility in increasing treatment specificity and reducing off-target effects associated with systemic administration[23]. For example, local controlled release of glucocorticoids and anti-proliferative drugs has been shown to reduce fibroblast proliferation and collagen deposition on pacemaker leads[24], stents, vascular grafts and biosensors[25,26]. Dexamethasone released from electrospun fibers[27] and drug-eluting sutures[28] decreases the foreign body response (FBR) and host rejection of biomaterials for various medical applications. Ketoprofen release from selectively permeable, porous microcapsules reduced post-transplant acute inflammation[29], and corticosteroid stabilized in viscous polymers has also yielded improved anti-inflammatory release[30]. However, despite improvements with locally integrated elution systems, the duration of many release strategies is limited to around 30–60 days, with the lack of longevity resulting in a delay with eventual resumption of immune and fibrosis responses once lingering effects of inhibition are lost[31]. Complicating factors include constant macrophage replenishment in the body[32] as well as the ability of macrophages to shift phenotype once the local microenvironment reverts to an untreated state[33]. As such, attempts to prevent implant rejection long-term, or utilize anti-inflammatory drugs for long term cell-based therapeutics, have remained challenging.

Controlled drug delivery through microencapsulation has been broadly explored, and typically involves an encapsulation material or device[34]. However, these devices are often made of materials that can themselves induce inflammation[6,35]. Furthermore, microencapsulation typically results in a device that is composed primarily of the encapsulation material, not the drug, limiting the amount of drug that can be included for a given volume[34]. Finally, there are many devices where function is desired for very long time periods, on the order of years, requiring the development of a very slow and compact drug releasing system[1–6]. We sought to address these challenges through the development of a controlled-drug delivery system based on drug crystal formation. Crystallization has largely been utilized to image essential protein folding and observe target-agent interactions[36], or, in more industrial fields, for purification purposes[37]. Crystallized drug formulations for controlled drug release have been described in the literature, however they have typically been used as nano to few micron surface coatings[38,39] or in carrier-based formulations with low encapsulation efficiencies and limited release duration from hours to weeks[40,41]. Crystalline materials have also exhibited advantages of enhanced chemical stability[42].

In the area of drug delivery, given that many CSF1R inhibitors and broad-spectrum anti-inflammatory agents are highly hydrophobic, creating difficulties for pharmacologists to solubilize and formulate them for delivery in non-toxic ways[43], we felt that utilization of such a strategy would enable large concentrated, pure drug reservoirs to be delivered in a highly localized manner for long-term release. Herein, we report the development of compact solvent-free crystalline anti-fibrotic drug formulations for localized long-term delivery. These crystal formulations were shown to enable long term function in the absence of fibrosis in a range of devices including, alginate encapsulated cells, electrode-based continuous glucose-sensing monitors (CGMs), and muscle-stimulating devices (MSD). Long-term anti-fibrotic efficacy and implant utility were maintained across multiple implant sites—subcutaneous (SC), intraperitoneal (IP) and intramuscular (IM). These studies were performed in a range of animals, including SKH1 mice (SC), healthy and diabetic (STZ-treated) C57BL/6 mice (IP & SC), Sprague-Dawley rats (IM) and non-human primate cynomolgus monkeys (IP & SC). Initial studies were performed using rodent strains that had previously been investigated as model systems for fibrosis[10–12], and further validated in non-human primates.

Macrophage-targeted agents with anti-fibrotic activity –

From the literature we identified 12 immuno-modulating drugs either with known history or the potential to block fibrosis locally[10,14,23,24,27,44,45]. This list included some broad-spectrum anti-inflammatories, as well as agents targeted to essential macrophage biology pathways (Fig. 1). To investigate the effect of macrophage immunomodulation on FBR, we fabricated Ba^{+2}-cross-linked SLG20 alginate hydrogel spheres with these drugs, prepared as amorphous formulations (Supplemental Fig. S1a). Drug-containing spheres (500 μl/animal) were then implanted into the IP space (relevant for encapsulated islet biomass transplantation or placement of devices such as ports, catheters/cannulas, and meshes) of C57BL/6 mice (n = 5/group) for 14 days. Afterward, spheres were retrieved and analyzed for cellular deposition and fibrosis (Fig. 1 and Supplementary Fig. 1b-c). Dark field phase contrast images from harvested spheres show a marked reduction in cellular deposition on spheres in numerous drug groups (Fig. 1a and Supplementary Fig. 1b). This deposition on spheres was examined further with confocal for DAPI (nucleus marker), F-actin (cellular cytoskeleton marker) or macrophage marker CD68, and alpha-smooth muscle actin (α-SMact, myofibroblast marker) (Fig. 1a and Supplementary Fig. 1c).

Macrophage cell phenotype can be characterized through gene expression analysis of factors that correlate with macrophage activation[46]. To better understand macrophage responses as a function of different amorphous drug encapsulated within implanted alginate spheres, we used NanoString multiplexed gene expression analysis to profile host-mediated innate immune recognition following 14-days of implantation (Fig. 1b). Fibrosis-associated macrophage phenotypes and corresponding fibrotic response correlated as numerous drugs inhibited host response to varying degrees (Fig. 1b, *green*), as compared to no drug (blank) and vehicle-loaded (DMSO) controls. Inhibitors with similar targets induced similar phenotypes, and most showed significant reduction of inflammatory macrophage markers Sphingosine Kinase 1 (Sphk1), Tumor Necrosis Factor α (TNFα), Arginase 1 (Arg1), and Interleukin 1 (IL1)[33,46]. Activated myofibroblast marker α-SMact and fibrosis marker Collagen 1a1 (Col1a1) were also decreased on the surface of numerous drug-encapsulating hydrogel implants, in a similar fashion, as compared to fibrosed controls. Corroborating observed decreases in expression of macrophage marker CD68 on drug eluting capsules (DEC), flow cytometry confirmed significant decreases in adherent macrophagesand neutrophils (Fig. 1c), as compared to those on no drug (blank, *red*) and DMSO vehicle (*black*) implants. Remaining drug extracted from retrieved capsules indicated less than 5% was found attributing the observed activity to the vast majority of payload release (Fig. 1d). The pharmacological agents with the highest anti-fibrotic efficacy, including CC-5013, dexamethasone, QNZ, Ly2157299, curcumin, Ki20227, GW2580, were chosen as a focus for the development of long-releasing formulations.

Design of crystalline drug formulations for long-term release –

To enable long term anti-fibrotic function in vivo, we sought to develop compact crystal formulations to allow long-term, controlled release with high drug density (Fig. 2a). Various techniques have been reported in the literature for compound crystallization including the use of additives and co-crystals[39]. Here, we have examined three different techniques to induce crystallization using GW2580 as a model compound: I) solvent evaporation (MI), II) temperature-induced (MII), and III) solvent/anti-solvent mixture (MIII) (Supplementary Fig. 2). Solvent evaporation resulted in low reproducibility of crystal structure, including random crystallization and large fractions with twinning (Supplementary Figs. 2a and 3a). The second (temperature-induced) technique, MII, produced crystals with a wide size range as well as solvent molecules in their lattice (Fig. 2b and Supplementary Figs. 2a and 3b-d). Alternatively, solvent/anti-solvent mixture of polar/non-polar solvents (MIII), specifically ethyl acetate/n-hexane was found to be a reproducible method for producing compact crystals with a more controlled range of crystal size and a crystalline lattice free of solvent (Fig. 2b and Supplementary Figs. 2 and 3b-e). A range of different parameters was explored including drug concentration, solvent mixtures, processing time, and temperature to identify conditions that enabled a pure drug crystal formulation, with no additives and an ordered crystalline structure (Supplementary Fig. 4). Crystals from both techniques MII and MIII were found to behave differently upon contact with aqueous media, attributable to the differences in their crystalline lattice structure (i.e., presence (MII) vs. lack of solvent (MIII)) (Fig. 2c and Supplementary Figs. 2b and S3b-d, and Supplementary Video 1). MIII crystals were found to exhibit higher thermal stability than MII as found by DSC and TGA (Supplementary Fig. 3e-f). A single sharp melting temperature peak was identified at 216.40°C indicating a pure fraction of compact crystals, while MII crystals exhibited 2 peaks at 145°C and 189°C attributed to DMSO followed by crystal collapse and melting[47,48] (See Supplementary Discussion 1).

Determining the Mechanism of Drug Release –

We aimed next to examine drug release of GW2580 from crystals prepared by both methods: (MII)–Crystal form 1 (F1), and the highly compact from MIII–Crystal form 2 (F2). Towards determining the different rates of release of drug forms F1 and F2, we employed *in situ* time-resolved atomic force microscopy (AFM) (Supplementary Fig. 5)[49]. This technique enabled us to monitor the real time release of molecules from their crystal surfaces under physiological conditions. Crystals were placed in an undersaturated phosphate buffer (PBS) solution at 37°C and sequential AFM images were collected. To compare release rates, we monitored the crystal surface for F2 (MIII) versus F1 (MII) (Figs. 2d & e, and Supplementary Fig. 5), and for F2 (MIII) as a function of crystal size (Fig. 2f). We identified significant differences in the mechanisms by which molecules are released from F1 and F2. On the (001) F2 crystal surface we observed the formation of monomolecular height and larger (>10 nm) etch pits (Fig. 2d and Supplementary Fig. 5d). Overall, our *in situ* observations indicated that F2 crystals dissolve by surface dissolution and etch pit expansion leading to slow surface release. In contrast, F1 crystals collapsed at the grain boundaries after immersion at 37°C, resulting in a burst of drug release (Fig. 2c-e, and Supplementary Figs. 2b and Fig. 5d). Following this initial collapse, F1 crystals were observed to dissolve from the edges of the grain boundaries and no single steps were observed on the (001) faces. Importantly, we noted that F2 crystals are stable during *in situ* conditions over extended time periods and can enable controlled release (See Supplementary Discussion 2).

Identification of crystalline properties and polymorphism –

Crystals developed by MIII were found to have uniform (single polymorph) repeating crystalline units as confirmed by PXRD and different from their amorphous form as shown by SEM (Fig. 2a and 2g). In addition, a number of internal molecular interaction properties resulted from this formulation strategy, as confirmed by SXRD (Fig. 2b). This method was also used to form compact crystals with drugs Ki20227, QNZ, dexamethasone, curcumin, and CC-5013, all having similar density, single polymorphism, and crystalline packaging (Fig. 2h and Supplementary Figs. 6 and 7). This formulation methodology yielded higher than average crystal structure packing density with non-hydrogen atom volumes ranging 15–18 A^3 calculated by SXRD, as compared to ~18–21 A^3 for most of the pharmaceuticals[50,51]. We believe these compact properties derive from prominent interaction interfaces between hydrophobic components inside the crystalline lattice and hydrogen bonding between crystalline repeating units.

Drug encapsulation and release rate –

Crystals were mixed in alginate solution and then encapsulated using an electrospray gelation system as previously reported[11]. Flow rate, voltage and alginate concentration was optimized for uniform capsule formation as detailed in the methods section. First, we examined release as a function of the percentage of crystallinity in the capsules. Pure crystalline, amorphous or crystalline/amorphous mixtures were encapsulated and release was examined for 2 months (Supplementary Fig. 8). In another study, release was examined after encapsulation of pure crystal formulations with different size ranges, or as a mixture with amorphous drug, under accelerated release conditions (Fig. 3a-b and Supplementary Fig. 9 and 10a-b). In general, controlling the ratio of drug form and crystal size or size range allowed for control of release rates.

Crystallized drugs months-long anti-fibrotic effects in vivo –

Leading drug candidates identified for their anti-fibrotic potential (Fig. 1) were crystallized, encapsulated in 500 μm alginate spheres, and then implanted into the IP space of C57BL/6 mice for long-term testing (Fig. 3c-3j). These capsules were retrieved after 1, 3, and 6 months and analyzed for cellular deposition and fibrosis. Interestingly, all capsules containing drug crystals were fibrosis-free, as determined by phase contrast imaging and confocal microscopy (Fig. 3c and Supplementary Fig. 10c-d). Control alginate spheres without drug exhibited fibrosis at 1 month and extensive clumping at 3- and 6-months post-implant (Fig. 3c). FACS analysis of cells isolated from retrieved capsules indicate reduced innate immune cell presence on the surfaces of retrieved crystalline drug-loaded capsule groups, even 6 months post-implantation (Fig. 3d and Supplementary Fig. 10e). Remaining drug crystals were found in retrieved capsules even after 6 months (Fig. 3e, i-j and Supplementary Fig. 11).

In order to confirm anti-fibrotic efficacy in another implant site, histological staining (Masson’s Trichrome and H&E) of capsules placed in the subcutaneous space revealed that capsules with drugs have significantly reduced cellular infiltration and fibrotic (collagen) deposition following 3 months (Fig. 3f). FACS analysis of cells taken from retrieved and dissociated SC tissues with capsules confirmed significantly reduced macrophage levels on and around implants (Fig. 3g). To determine whether fibrosis-free capsules were due to local or global immunomodulation, plasma drug concentrations were monitored throughout the study by LC-MS. Interestingly, drug levels were below the reported drugs IC_{50}s (2.5–21 ng/ml) (Fig. 3h) and also below detection limits within 1 to 2 weeks post-implantation, depending on whether capsules were placed into IP or SC sites. This indicates that the observed anti-fibrotic effects are likely due to localized as opposed to systemic immunosuppression. Drug extraction analysis by HPLC also determined that a notable percentage of the loaded drug, especially for SC samples, remained within explanted capsules (Fig. 3i-j), suggesting that fibrosis prevention could continue for a longer period of time.

Drug release and anti-fibrotic effects in non-human primates –

Next, we wanted to confirm whether these findings, which include multiple implant sites, could translate to a higher order species. Leading drug GW2580 was formulated as crystals and encapsulated in both 0.5 and 1.5 mm SLG20 alginate capsules for IP and SC implantation in healthy non-human primates (NHPs) as previously reported[12]. Implants were then retrieved at 2, 4 weeks and 3 and/or 6 months (Fig. 4 and Supplementary Fig. 12 and 13, and Supplementary Videos 2 and 3). 0.5 mm-sized drug-loaded capsules remained fibrosis-free and largely unattached in the IP space up to 1 month and in the SC site up to 6 months post-implant, while 1.5 mm drug-loaded capsules remained clean in both implant sites for 6 months (Fig. 4 and Supplementary Fig. 12). Fibrosis-free capsules were freely dissociated from either IP omentum following peritoneal lavage during minimally invasive laparoscopic retrieval or SC tissue by biopsy punch[12]. Using phase contrast, brightfield and laparoscopic imaging, retrieved 0.5 mm (up to 1 month) and 1.5 mm (up to 6 month) capsules appeared translucent with visible, remaining encapsulated crystalline drug and free of cellular overgrowth (Fig. 4a & d, and Supplementary Fig. 12a-d). Correlating with the extent of FBR, remaining drug was extracted from retrieved capsules and quantified by HPLC, showing additional stores in 1.5 mm capsules in both the IP and SC sites up to 6 months, while 0.5 mm capsules only had remaining drug in the SC site at 6 months but little to no drug by 3 months in the IP space (Fig. 4b), suggesting faster release in the more aqueous IP compartment. Drug concentration in IP lavages was also measured at each capsule retrieval time point by LCMS, and was found to drop from 2–3 ng/ml to below detection limits (0.5 ng/ml) following 4 weeks post-implantation for 1.5 mm capsules (Fig. 4c). Plasma analysis at the end of the study showed GW2580 levels below detection limits. Cells present on retrieved capsules were dissociated, stained, and analyzed by FACS. Capsules with GW2580 showed significant reduction of macrophage responses when drug was remaining (Fig. 4e).

Cryo-SEM analysis for the capsules pre- and post-transplantation (Supplementary Fig. 13) revealed no topographic changes on the capsule surface, and show crystals shrinking with time into the surrounding crosslinked alginate matrix. As expected from previous studies in NHPs[12], 0.5 mm blank capsules implanted IP were irretrievable due to attachment to the peritoneal wall (Supplementary Figure S9 in Ref. 12), thus limiting external comparison to 0.5 mm drug-loaded capsules. In order to analyze capsules without drug, we performed histology on omental tissues containing fibrosed and embedded capsules which were excised from the site of implantation at the same timepoints. Excised tissues obtained from the implant sites of drug-loaded 0.5 and 1.5 mm alginate capsules were examined through histological staining analysis (Masson’s Trichrome and H&E), which confirmed the lack of sphere embedding and collagen deposition over the same timeframes (Fig. 4f-g and Supplementary Fig. 12e-f). Moreover, while 0.5 mm drug-loaded capsules became clumped at 3 months due to low remaining drug stores, they were not extensively embedded into surrounding omental tissue until 6 months (Fig. 4a, 4e-g and Supplementary Fig. 12b, e-f).

Lastly, NanoString multiplexed gene expression analysis was performed to profile host-mediated innate immune recognition of SC drug-loaded capsules vs. that of blank capsules retrieved 4 weeks post-implantation (Fig. 4h). Similar to B6 mouse model responses (Fig. 1b)[10,33,46], significant reduction of inflammatory macrophage markers Sphk1, TNFα, Arg1, and IL1, among others, was observed. We believe that further increases in crystal sizes would result in even longer release times.

Crystalline GW2580 with β-cells in diabetic mice –

We next investigated whether observed improvements in biocompatibility through crystalline drug encapsulation could yield improved/prolonged function of an implanted biomedical device with living cells (Supplementary Fig. 14). Lead drugs from (Fig. 1) were screened for lack of toxicity *in vitro* against both immortalized murine macrophage RAW264.7 cells shown by CellTiter-Glo (Supplementary Fig. 15) and against encapsulated rat islets to study the potential for impact on islet biology and function (Supplementary Fig. 16 and Supplementary Discussion 3). We evaluated rat islet function within 0.5 mm microcapsules without drug, compared to islets within 0.5 mm capsules with co-encapsulated lead candidate crystalline GW2580, after transplantation into STZ-induced diabetic C57BL/6 mice. Previously, it has been shown that 0.5 mm-sized SLG20 alginate capsules result in encapsulated islet graft cell death and loss of normoglycemia in the same model[44,52]. First, we determined that GW2580, in two forms–amorphous and crystalline, is non-toxic to co-encapsulated rat islets, at all drug loads tested (Fig. 5a and Supplementary Fig. 17a). Both drug formulations were capable of preventing loss of glucose correction for extended periods of time following transplantation into the IP space of diabetic mice (Fig. 5b). Controls (Fig. 5b, *red trend*) failed, on average, by ~35 days, while amorphous (Fig. 5b, *blue trend*) and crystalline (Fig. 5b, *green trend*) formulation-loaded capsules maintained normoglycemia for either over 70 days or, much more significantly, at least 15 months or 460 days at which time mice were terminated to analyze capsules. Macrophage depletion by clodrosome in combination with islets encapsulated in 0.5 mm SLG20 alginate islets but without drug prevented fibrosis and allowed for islet function, but induced significant toxicity by ~50–60 days post-transplantation (Fig. 5b, *purple trend*).

Explanted amorphous and crystalline drug-containing capsules were imaged (Fig. 5c) and analyzed for rat islet function/viability marker Pdx1 and host α-SMact expression at ~430 or 460 (~1.3 years) days post-transplant, respectively, for amorphous and crystalline GW2580 (GW) groups (Fig. 5d). Crystal GW2580 capsules had significantly higher islet viability, as indicated by ~30-fold higher Pdx1 expression, and lower myofibroblast and fibrosis response, as indicated by 74% lower α-SMact expression. The difference in Pdx1 was greater than that previously observed with larger 1.5 mm diameter capsule size alone[12], and cures were also elongated from ~6 months with 1.5 mm capsules to over 15 months with 0.5 mm drug-loaded capsules. Remaining crystalline formulated drug was also observed by microscopy within explanted capsules at 460 days (Fig. 5c). Lastly, by drug extraction and HPLC quantification we have found up to 27.3% of crystalline GW2580 dose remaining in islet-containing capsules after 460 days, indicating the potential of longer term function.

Crystalline GW2580 with human islets transplanted SC and IP –

To our knowledge, islet transplantation into an unmodified SC site (more accessible for transplantation and subsequent manipulations or replacement) has never reversed diabetes in fully immune competent animals or humans[53]. It has been hypothesized that this environment is inhospitable to cell survival due to inadequate vascularization and poor oxygen tension[54]. Strategies for SC transplantation based biomaterials also face the additional challenge of the fibrotic response to the encapsulating material. Physical interactions with host blood, lymph, exudate or other fluids can lead to adsorption of proteins onto the implant, including albumin, complement, fibrinogen, γ-globulin and fibronectin and eventual inflammatory response[53].

Human islets were encapsulated in 0.5 mm microcapsules, with and without crystalline GW2580, and transplanted into the IP space or injected subcutaneously in STZ-induced diabetic C57BL/6 mice. For SC delivery, the capsules were placed in 2 separate and elongated locations, one on each side of the animal (Supplementary Fig. 18). We hypothesized that distributing the encapsulated cells to multiple locations could reduce the oxygen and nutrient demands at each site. GW2580 in crystalline form was found to be non-toxic to co-encapsulated human islets at the same drug load of 10 mg drug/ml alginate

(Supplementary Fig. 17b). As compared to control (no drug) capsules, drug-loaded capsules in both IP and SC sites were equally capable of restoring glycemic control in diabetic mice for extended periods of time up to 72 days (Fig. 5e, *gold and teal trends*), at which point in time the experiment was terminated to analyze samples. In contrast, SC capsules without drug did not provide control of blood sugar. (Fig. 5e, *red trend*). These same capsules in the IP space failed after ~32 days, presumably due to the fibrotic response (Fig. 5e, *green trend*). Capsules without drug placed in the SC space were fully fibrosed, surrounded by a solid collagen sack of disk-like due to capsules individually fibrosis (Fig. 5f).

Fibrosis prevention with crystalline GW2580 in PDMS discs –

To examine whether crystalline-formulated drug could reduce the fibrotic response to other materials, we mixed crystalline GW2580 into polydimethylsiloxane (PDMS) at 0, 1, 5, or 10% w/w prior to curing into discs (Fig. 6a and Supplementary Fig. 19a). This was done to first establish anti-fibrotic efficacy within a known single biomaterial PDMS, FDA-approved for numerous device systems including breast implants and cannulas, for which SC and IP sites are more relevant for biocompatibility and drug release assessment. Discs with and without GW2580 were then implanted both IP and SC for 2, 4 weeks, and 3 months in C57BL/6 mice (1 disc/site/mouse). FBR, observed as yellowish-pink tissue on retrieved PDMS discs, was reduced in a dose-dependent fashion by all drug concentrations at 2 and 4 weeks as well as 3 months (Fig. 6a and Supplementary Fig. 19b-c). Masson’s Trichrome and H&E histological staining of both excised SC and IP samples confirmed significantly reduced immune cell infiltration and fibrosis, as compared to blank (no drug) control discs (Fig. 6a and Supplementary Fig. 19c). Determination of remaining drug levels by HPLC, following either SC or IP implantation for all time point incubations, once again confirmed that release was slower in the SC space (Fig. 6b). Flow analysis for responding macrophages dissociated from retrieved discs showed significant reductions in cell numbers between drug-containing discs and no drug controls at all-time points for IP implantations, and at 2 weeks and 1 month for SC implantations (Fig. 6c). While macrophage levels remained low for all drug-containing discs at 3 months, levels detected on control (no drug) discs significantly decreased over time, resulting in a lack of relative difference at 3 months in the SC space. We have observed this phenomenon of decreasing immunologic engagement over time for other untreated material implants at late (>2–3 month) time points (Fig. 3d and 4e). As fibrotic encapsulation becomes more complete, macrophage density around the implants decreases. Drug retention was also much higher in PDMS as compared to alginate hydrogel capsules, over the same incubation times, mainly due to limited swelling ability (Fig. 6b vs. Fig. 3j).

Crystalline GW2580 along with multicomponent devices –

The utility of crystalline GW2580 was also evaluated with multicomponent devices comprised of different materials including plastic composites, metal alloys and enzymes. Two different implants models were tested: 1) devices-sensors for collecting information from the host and 2) devices that employ a function onto surrounding host tissues. We chose CGM Enlite sensors (2nd generation) and an in-house-manufactured muscle stimulating device (MSD), (Supplementary Fig. 20a and Fig. 6d-f, Supplementary Fig. 20b and Fig. 6g-j, respectively). Drug crystals were add to fast thermo-curing Polyimide (PI)[55] and applied as top coatings onto the implantable part of each device (Supplementary Fig. 21 and Supplementary Discussion 4). Coated CGM sensors were studied in their clinically relevant site of use (SC) in hairless SKH1 mice, which show intact subcutaneous inflammation and fibrotic responses similar to C57BL/6 mice[11] while not requiring additional shaving and use of Nair to remove signal detection interference[10], with IVIS whole body imaging for implant-induced inflammation at 1, 4, & 7 days post-insertion. The incorporated crystals significantly reduced implant-induced inflammation (Fig. 6d). Following 4 weeks, sensors were retrieved and analyzed. As opposed to no drug controls, crystalline GW2580 drug-coated CGMs had little to no fibrotic encapsulation, as determined by histological staining (Fig. 6e-f). Crystalline GW2580 efficacy in a second multi-component MSD model was also evaluated at a different implantation site, i.e. intramuscular (IM). In our model the inflammation/immune and fibrosis responses persist, specifically in the gastrocnemius and bicep muscles which are the immediately adjacent tissues. As such, MSDs were sutured to gastrocnemius muscle of Sprague-Dawley rats, relevant for muscle atrophy studies, following severing of the tibial nerve, and daily muscle stimulation was performed for 2 weeks starting at 3 days post-implantation. Devices were retrieved at 17 days. Control MSDs without drug were associated with thick fibrosis for controls (>500 μm), while GW2580-coated MSDs had no significant fibrosis (Fig. 6g). This was confirmed by H&E-stained histological sections of surrounding muscle tissues, showing substantial reduction of fibrosis along with a larger density of muscle fibers with drug-loaded MSDs (Fig. 6h). Quantitative gene expression analysis on the device and surrounding muscle indicated reductions of macrophage marker CD68, fibrosis marker α-SMactin, and inflammatory TNFα for crystalline drug-coated MSDs (Fig. 6i). Device function enhancement was also confirmed by quantitative analysis of muscle atrophy (Fig. 6j). Less muscle atrophy was found when drug-loaded MSDs were used, likely due to prevention of the fibrotic capsule and improved stimulation and enervation of the surrounding tissue.

In summary, we have developed crystalline, anti-inflammatory drug formulations that are capable of providing local, long-term, non-toxic control of fibrosis. Release kinetics of these drugs could be tuned by controlling several parameters including crystalline degree, compositions, crystal form, crystal size and morphology. The compact nature of these crystals is supported by hydrophobic chemical moiety interactions and inter and intra molecular hydrogen bonds, limiting the rate of infiltration by water resulting in slow release through surface erosion/dissolution. We demonstrate the potential of this approach with a number of anti-inflammatory drugs, and importantly identify formulations that can be utilized for slow release over months to years.

One crystal formulation of particular interest is GW2580, a CSF1R small inhibitor, which we demonstrate has the potential to provide local control of fibrosis in a range of settings. When encapsulated in alginate microspheres, crystalline GW2580 could suppress fibrosis in both rodents and non-human primates (Figs. 3 and 4). When islets were included in these formulations, these capsules were able to provide long term control of blood sugar in diabetic C57BL/6 mice, with both human and rat islets (Fig. 5). Interestingly, these formulations allowed for significant, albeit imperfect, control of blood sugar following placement in the subcutaneous space. To our knowledge this is the first demonstration of a formulation capable of providing blood sugar control with human cells in C57BL/6 mice subcutaneously. Finally, we demonstrate that crystalline, GW2580 was able to significantly reduce the fibrosis and improve performance on two different multi-component devices, a continuous glucose monitor and an electrical muscle stimulation device (Fig. 6). We believe the formulations described here could have utility in a range of device applications including cellular transplantation, implantable stimulators and sensors, and prosthesis for tissue engineering.

METHODS AND MATERIALS

Materials

In vitro reagents purchased from Life Technologies (Carlsbad, CA), unless otherwise mentioned. The antibodies (Fluor-conjugated anti-mouse Ly-6G/Ly-6C (Gr-1), CD11b, and CD68) were purchased from BioLegend (San Diego, CA) and used as described below. For non-human primates immunostaining, anti-human CD68 antibody Alexa Fluor-conjugated was purchased from Santa Cruz (Dallas, TX). The CD11b (anti-mouse/human) antibody (from BioLegend-San Diego, CA) was used the same for both mouse and primate staining. The 425–600 μm acid washed glass spheres (Cat#/Lot#: G8772/SLBL7288V) and Cy3-conjugated anti-mouse α-SMact antibody were purchased from Sigma-Aldrich (St. Louis, MO). The Dow Sylgard 184 silicone elastomer-PDMS curing kit, was purchased from Dow Corning, USA (Midland, MI). Alginate-PRONOVA SLG20 was purchased from NovaMatrix (Sandvika, Norway). Materials used in this study were tested for endotoxin content by a commercial vendor (Charles River, Wilmington, MA), and found that spheres contained endotoxin levels below the detection limit (< 0.05 EU/ml). PI 2525 was purchased from HD Microsystems. All the solvents were analytical grade and purchased from Sigma-Aldrich, USA. Sodium dodecyl sulfate (SDS) was purchased from Sigma-Aldrich, USA. Drugs were purchased from various vendors: rapamycin and dexamethasone (Sigma-Aldrich), GW2580 (LC Laboratories), LY2157299 and QNZ (Cayman), curcumin (Enzo), Ki20227, A83–01 and D4476 (Tocris), CAL-101 and lenalidomide/CC-5013 (Selleck Chem), and cFMS Receptor Inhibitor III (EMD Millipore).

Preparation of crystals

In this study three different crystallization techniques (MI-MIII) were used for crystals preparation and the resulting crystals were confirmed by microscopy methods and X-Ray Diffraction (XRD) for lattice structure, density and polymorphism.

MI: Solvent evaporation induced crystallization, drugs were solubilized in acetone in under-saturated levels and then solvent was allowed to be evaporated at room temperature allowing crystals to form. Crystals were harvested and analyzed as mentioned above. A wide range of crystal sizes was obtained, along with the major portion of crystals characterized with twinning.

MII: Temperature induced crystallization, drugs were solubilized at oversaturation in DMSO using heating 50–120ºC followed by fast cooling to room temperature or to 4ºC, then solutions were kept from 30 min-24 hours to complete crystal growth. Crystals were harvested and analyzed as mentioned above.

MIII: crystallization in solvent:anti-solvent mixture, all crystals were grown at constant temperature (20–30ºC) using solvent:anti-solvent mixing methods with concentrations range: 0.001-to-5000 mg/mL of hydrophobic compounds, where the anti-solvent is added into portions. Ethyl acetate (EA) was used as a solvent while Hexane (HE) as an anti-solvent. For example, hydrophobic compounds, particularly, 100 mg of Curcumin, 100 mg of Dexamethasone, 100 mg of Ly215799, and 100 mg of GW2580 were each initially dissolved in 5 to 150 ml EA. In some crystallization experiments, solvent solutions were sonicated up to 15 minutes and/or pre-heated in a range from 20 to 80°C to facilitate solubility. To the solutions of each of these hydrophobic compounds HE was added into sub-portions to fit a range of 0 to 150 ml/100 mg dissolved hydrophobic compound in EA, depending on the desired final crystal size range. Resulting mixtures were then incubated at stable temperature i.e. 20–30°C. The process was optimized for minutes to hours depending on molecular structure of the compound, and desired crystal size range; for example, 100 mg of dexamethasone was dissolved in 40 ml EA, and 30 ml of HE was added and the process was fit to 4 hours, yielding crystals with a size range 40–80 µm. Controlling crystal size depends on various conditions that need to be optimized, i.e., drug concentration, solvent:anti-solvent ratio, temperature, process-time etc.

Amorphous materials preparation:

Amorphous form was prepared for drugs in this study by 2 methods depending whether cells were encapsulated with drug or not:

With no cells in encapsulation: The amorphous material was prepared inside the polymer solution (hydrogel) by first dissolving the drug in DMSO (in a minimum volume), then the dissolved drug was added to the polymer solution to fit a desired drug concentration per ml of mixture (with the vast majority of the mixture volume, ≥ 70%, by volume, being aqueous). By mixing, the two solvents interfere and uniformly push the drugs quickly out of the DMSO to be trapped inside the aqueous solution/hydrogel/polymer matrix in an amorphous form, with drugs being finely dispersed inside this mixture. The amorphous % yield is ≥ 90% (due to self-crystallization in some cases). This suspension/mixture was further encapsulated to make capsules release drug in a burst manner (days to couple of weeks duration). Amorphous-based formulations were prepared fresh before implantation to avoid self-crystallization due to limited stability.

This method can be applied to any homogeneously able-to-be-mixed solvent system where the first solvent is the drug solvent and the second is anti-solvent (where an encapsulating polymer may be dissolved, or not, and where the anti-solvent is the major constituent in the final mixture: ≥ 70%). Fig. S1a shows representative amorphous formulations prepared *in situ* by this method inside hydrogel alginate.

When cells are involved in the encapsulation process: To a glass vial fixed on a hot plate (40–50ºC) continuously flushed with N_2 or Ar, a saturated drug solution (drug + minimum volume of solvent) was added in a droplet manner. By first contact between the drug solution and hot glass surface the solvent immediately evaporates and results with the drug in amorphous form. The fast-produced amorphous drug, in white powder form, was immediately collected and used for co-encapsulation with cells. The amorphous % yield is ≥ 70% (due to self-crystallization in some cases and how fast evaporation occurs depending on the solvent). Also in this case, amorphous-based formulations were prepared fresh before implantation to avoid self-crystallization due to limited stability.

Single crystal x-ray diffraction (SXRD) and powder x-ray diffraction (PXRD)

SXRD - For all structures, intensities were recorded using a Bruker-AXS X8 Kappa diffractometer, performing φ- and ω-scans. The instrument was equipped with a Bruker APEX2 CCD and an Oxford Cryosystems CryosStream 700 Plus set to 100K. The diffractometer was further equipped with two IμS microsources emitting Mo K_α radiation (λ = 1 0.71073 Å) or Cu K_α radiation (λ = 1.54178 Å). The programs SAINT[56] and SADABS[57] were employed for data reduction and scaling, respectively. The program SHELXT[58] was used to solve the phase problem and the program SHELXL[59] was used for structure refinement against F^2 on all data. Generally established refinement methods were employed[60]. All atoms (except hydrogen) were treated as anisotropicall. Hydrogen atoms on carbon were placed in their calculated positions and refined using a riding model. Hydrogen atoms on nitrogen or oxygen were located in the difference density map and were refined using distance restraints with target values of 0.84(2) Å for O—H and 0.91(2) for N—H distances. The U_{iso} values of all hydrogen atoms were constrained to be 1.2 or 1.5 times the U_{eq} of the atoms to which they bind. Some structures contained disorders. Those disorders were refined using similar distance restraints for bonds and angles. In addition similarity and rigid bond restraints were employed for the thermal parameters of disordered atoms.

PXRD - Powder diffraction experiments were carried out at low temperature (100K) with Cu Kα radiation (λ = 1.54178 Å) using a single-crystal diffractometer (Bruker-AXS X8 with APEX2 detector; the same instrument was used for the single-crystal data collections as well). The powder samples were held in a polyimide capillary that was rotating around its axis during data collection.

In situ accelerated release microscopy monitoring

GW2580 Crystals form samples were placed on glass slides with glass cover slips separated by selotip. To these samples, phosphate buffered saline solution (PBS) + 0.3% (w/v) SDS (to expedite the dissolution rate) was added, incubated at 37°C and *in situ* monitored. For the microscopy monitoring purpose we have used the DeltaVision Elite Widefield Deconvolution System (GE Healthcare) with filters: excitation 475nm, emission 525nm = Standard FITC/GFP filter set with objective lens: 10x, 0.4NA Plan Fluor. Samples were monitored for 24h at 37°C.

Ex situ and in situ Atomic Force Microscopy (AFM)

AFM - We employed time-resolved AFM as a technique to study on the molecular level the mechanism of drug release. Single crystals were prepared for *ex situ* and *in situ* observation in air and in solution to identify the dominant drug release mechanisms as well as to determine the kinetics between crystal forms. We employed a Cypher ES Environmental

AFM from Asylum Research (Santa Barbara, CA) for all experiments. The sealed liquid cells for the Cypher AFM are specifically designed with materials that are compatible for harsh solvent conditions. This AFM provides the ability to probe samples with environmental control, including precise temperature control with the modular sample stage. In this way, we were able to monitor drug release in ambient conditions (T = 25°C) during *ex situ* measurements prior to *in situ* wherein we increase and maintain T = 37°C during solution exchange.

Attachment of Crystals for AFM.—AFM measurements were performed with crystal forms 1 and 2, F1 (MII) and F2 (MIII) respectively, were crystals fixed on an epoxy substrate. Single crystals were attached using a thin film of partially-cured epoxy (MasterBond EP21AOLV) on Ted Pella 15 mm metal disks. The epoxy was partially cured at 60°C for 30 minutes prior to depositing the crystals using a statically charged pipette tip. All crystals were used for *in situ* observation within one hour of sample preparation.

In situ AFM Image Collection.—AFM images were collected via Olympus TR800PSA probes (Silicon nitride-probe: (5/30) Cr/Au coated and spring constant: 0.15 N/m) with a contact mode and ca. 32 kHz as a tapping frequency. Image sizes ranged from 1 to 10 μm with scan rates between 2 and 5 Hz, and 256 scan lines/image. Height and deflection imaging modes were employed for data analysis and image selection. We processed height and deflection images by 2nd order flattening and image contrast adjustment. No low pass, median, or 2D fast Fourier transform (FFT) filters were applied to any of the AFM images.

In Situ Monitoring of the Mechanism of Drug Release.—We attached single crystals to AFM sample pucks using epoxy, as described above, on the same day that we conducted the experiments. The sample were placed on the AFM scanner which was initially at 25°C. *Ex situ* images were collected of the (001) F1 and F2 crystal surfaces at T = 25°C prior to introduction of solution. From these AFM images, we identified the crystal edges in order to determine the crystallographic directions on the upward-facing (001) crystallographic faces for both F1 and F2 crystals.

We loaded the AFM fluid cell with reagent-grade PBS was allowed to thermally equilibrate to ambient temperature prior to being introduced into the AFM liquid cell. The solution was fully undersaturated upon being introduced. Upon introducing the undersaturated PBS, the temperature was set to T = 37°C and was maintained at a constant *in situ* temperature for the duration of the experiment. We recorded the time between introducing the solution, heating until thermally equilibration was achieved, and the AFM cantilever tip engaging with the surface, which we denoted by t_0. AFM images were continuously collected and the undersaturated solution was exchanged to maintain a constant degree of undersaturation. Different regions of each crystal surface was recorded, including the edges and the center of the basal (001) surfaces. Due to inherent drift that occurs with long time *in situ* AFM measurements, we show well equilibrated images of the surfaces over shorter time frames. These are representative of the full experimental time wherein we monitored the surface evolution for > ten hours, and in some cases exceeding 36 hours which is an extensive time for *in situ* AFM observations. All images were collected in contact mode; we verified that scanning in contact mode had no influence on the crystal's surface dissolution with increasing in the scan size at the end of each experiment and observing uniform changes across the entire scanned areas.

We measured the rate of drug release by measuring the negative step velocity v on the (001) surfaces. The displacement between step edges Δx were measured between sequential AFM height mode images. The time between images was recorded therefore we can quantify the step velocity as in Equation 1

$$v = \frac{\Delta x}{\Delta t} = \frac{x_2 - x_1}{t_2 - t_1} = \left[\frac{nm}{s}\right] \tag{1}$$

We quantify the drug release rate as proportional to the rate of molecules released for both F1 and F2. The rate of molecules released is proportional to the integral of the velocity over time, Equation 2,

$$n \propto l \int v \; dt \tag{2}$$

where l = a = 0.54 nm for F2, and the rate of molecules n released over time as shown by Equation 3

$$\frac{dn}{dt} = \quad \rho v l = \left(\frac{molecules}{nm2}\right)\left(\frac{nm}{s}\right)(nm) \tag{3}$$

We measured >20 independent steps for each crystal size and crystalline form. From this, we determined the negative velocities and sub sequentially, the rate of molecules released. Error bars were for all number of molecules released for each crystal surface. The calculated rate of molecules released were summed to demonstrate the cumulative rate of drug release as a function of time in an undersaturated PBS solution such that different drug crystals were comparable.

We quantify the initial release of molecules from F1 crystals by measuring the trough profile of the dissolution at grain boundaries on the F1 crystal (001) surface. The troughs are triangular in habit; we select a cross sectional area wherein the sectional volume is that of a triangle. The initial release of molecules is therefore proportional to the number of molecules released from this area. To approximate this for F1 we use that $l = \vec{a}\vec{c}$ where $\vec{a}$ and $\vec{c}$ lattice parameters (0.86 and 1.45 nm, respectively) to quantify the measured rate of release by the relationship in Equation 1. For line measurements after the initial release, we use $l = \vec{a}$ based on the measured velocities in the $\vec{a}$ direction. The $\vec{c}$ direction corresponds to the single line width of the measured sectional area.

Differential scanning calorimetry (DSC) and Thermogravimetric analysis (TGA)

DSC – The analysis was conducted using the thermal analyzer DSC 8000 (PerkinElmer). Studied samples were heated from 25-to-300°C at 10°C/min. Amorphous and crystal GW2580 (MII and MIII) samples were subjected to TGA under inert nitrogen atmosphere for avoiding undesired oxidation. The samples mass used in this study was 2–5 mg and Pyris

1 TGA analyzer (PerkinElmer) was utilized to follow mass changes in the studied samples, in response to temperature increase during the pyrolysis reaction were the thermogravimetric curves obtained with heating rates of 1°C/min and heating between 50 and 400°C.

Scanning electron microscope (SEM)

Crystal size, morphology, and topography were intensively studied with SEM. Samples were prepared for imaging by first placing them on conductive carbon paper and then coating with ~10 nm of Gold/Palladium (Au/Pd) using a Hummer® 6.2 Sputter Coater System. Coated samples were imaged using the JEOL-JSM-5600LV Scanning Electron Microscope with 2.0–15.0 KV acceleration voltage. For analysis purposes, three samples of each crystal preparation were studied as the following: three images were collected per sample and ten random measurements were applied per image.

Fabrication of alginate hydrogel spheres, with or without drug

Alginate hydrogel spheres were made as reported previously[10]. Simply, voltage generator was coupled to a syringe needle releasing alginate and grounded to a gelling bath vessel. Spheres were produced from sterile alginate (PRONOVA SLG20, NovaMatrix, Sandvika, Norway), 2% w/v solution, dissolved in 0.9% saline (pH 7.4). For the drug formulation-loaded spheres, drugs crystals or amorphous drug (both amorphous methods) were added to the dissolved alginate and mixed well. 500 μm diameter alginate hydrogel spheres were fabricated using a 23–25G blunt needle, 5–8kV voltage and a flow rate of 200–300 μl/min. Blank alginate or with drug was then crosslinked in 250 ml gelling solution of sterile $BaCl_2$ (20mM $BaCl_2$, 25mM HEPES, 250mM D-Mannitol, pH 7.4). Following gelation, alginate spheres were washed 4 times with HEPES buffer (25mM HEPES, 132mM $NaCl_2$, 1.2mM $MgCl_2$×6H2O, 4.7mM KCl, pH 7.4) and then 4 times with 0.9% saline, 40 ml each wash. Immediately following preparation, samples were implanted in vivo or tested in vitro to avoid any undesired self-crystallization (samples encapsulated amorphous drug) or initial drug release.

In vitro release from drug-loaded spheres (crystalline or amorphous):

Release studies were carried out in different media: depending on the studied drug; curcumin: phosphate buffered saline (PBS, pH 7.4) + 20% ethanol or normal saline + 20% ethanol, QNZ: PBS + 10% DMF, and GW2580: was studied in PBS and also under accelerated condition in PBS with SDS)0.1% or 0.3% w/v, as indicated(. Sink condition was maintained across all of the *in vitro* release studies. For curcumin and QNZ release studies a 100 μl of capsules loaded with 4 mg drug/ml, were incubated in 2 and 3 ml release medium respectively at 37°C. Sampling was done by total replacement of release media. Sampling time points were 10, 30 min, 1, 4, 16h, 1, 2, 3, 5, 7, 10 and 14 days, and then weekly, until completion of a 60-day period. For release in accelerated condition (PBS + SDS), the same time points were followed while 20 μl of capsules with 10 mg/ml drug were incubated in 2 ml release medium to achieve sink conditions. Sample drug concentrations were quantified using a UV-calibrated system or through reversed-phase HPLC equipped with C-18 column. A gradient mode with 1 ml/min of flow rate was applied and a different wavelength (nm) for each drug with 10–50 μl sample volumes being injected into an HPLC system (or UV analyzed-Tecan infinite M200 PRO). Calibration curves, ranged over 0.05–500 µg/ml (for most of the drugs, see below), and allowed for calculation of sample drug concentrations.

HPLC

Calibration curves were obtained on an Agilent 1100 Series HPLC instrument (Agilent Technologies, CA, USA) equipped with binary pump (G1312A), auto-sampler (G1313A), degasser and photodiode detector (DAD, G1315A). Agilent ChemStation Software was utilized for HPLC system control, data acquisition and processing. The chromatographic separation was performed with an analytical Waters Atlantis T3 C18 column (5µm, 4.6 × 250 mm). The temperature of column and auto-sampler were kept at 20°C. For all of the drugs, gradient mode with a constant flow rate (1 ml/min) was applied using a mobile phase consist of: (A) 0.1% formic acid (FA) in acetonitrile (ACN) and (B) 0.1% FA in water.

Stock solution of GW2580 (10 mg/ml) was prepared in dimethyl sulfoxide (DMSO) and appropriate dilutions were made in DMSO to prepare standards (0.25 – 2500 µg/ml) for calibration curve of GW2580. 10 µl of standard solution was injected with analytes eluted by gradient mode. Mobile phase gradient conditions: (0 min 10% A), (10 min 95% A), (14 min 95% A), (16 min 10% A), and (20 min 10% A).

Stock solution of Curcumin (10 mg/ml) was prepared in DMSO and appropriate dilutions were made in DMSO to prepare standards (0.05 – 500 µg/ml) for calibration curve of Curcumin. 10 µl of standard solution was injected with analytes eluted by gradient mode. Mobile phase gradient conditions: (0 min 70% A), (4 min 95% A), (10 min 95% A), (12 min 70% A), and (17 min 70% A).

Stock solution of QNZ (10 mg/ml) was prepared in DMSO and appropriate dilutions were made in DMSO to prepare standards (0.06 – 125 µg/ml) for calibration curve of QNZ. 50 µl of standard solution was injected with analytes eluted by gradient mode. Mobile phase gradient conditions: (0 min 20% A), (8 min 95% A), (12 min 95% A), (13 min 20% A), and (17 min 20% A).

Stock solution of LY2157299 (10 mg/ml) was prepared in DMSO and appropriate dilutions were made in DMSO to prepare standards (0.06 – 250 µg/ml) for calibration curve of LY2157299. 50 µl of standard solution was injected with analytes eluted by gradient mode. Mobile phase gradient conditions: (0 min 10% A), (7 min 60% A), (8 min 95% A), (12 min 95% A), (13 min 10% A), and (17 min 10% A).

Stock solution of KI20227 (10 mg/ml) was prepared in DMSO and appropriate dilutions were made in DMSO to prepare standards (0.06 – 500 µg/ml) for calibration curve of KI120227. 50 µl of standard solution was injected with analytes eluted by gradient mode. Mobile phase gradient conditions: (0 min 20% A), (7 min 75% A), (8 min 95% A), (12 min 95% A), (13 min 20% A), and (17 min 20% A).

Stock solution of Dexamethasone (10 mg/ml) was prepared in ethanol and appropriate dilutions were made in ethanol to prepare standards (0.06 – 500 µg/ml) for calibration curve of Dexamethasone. 50 µl of standard solution was injected with analytes eluted by gradient mode. Mobile phase gradient conditions: (0 min 50% A), (7 min 80% A), (8 min 95% A), (12 min 95% A), (13 min 50% A), and (17 min 50% A).

Islet isolation, purification, and encapsulation

Rat islets were derived from 300 grams (8–10 week old) male Sprague-Dawley rats (Charles River, Wilmington, MA) as previously reported[12]. Isolation surgeries were conducted following the early reported method[61]. Briefly, the bile duct was cannulated and the pancreas distended by an injection of 0.15% Liberase (Research Grade, Roche) in RPMI 1640 media. Until the completion of all surgeries, isolated pancreatic organs were kept on ice in conical tubes (50 ml). Following, sample tubes were placed in a 37°C water bath for 30-min digestions, and then stopped with addition of 10–15 ml cold M199 media (+ 10% HIFBS) with light shaking. Digested pancreases were then washed twice in M199/HIFBS media, filtered with a 450 μm sieve, and suspended in a Histopaque 1077 (Sigma)/M199 media gradient for centrifugation at 1,700 RCF at 4°C. Depending on the gradient islet layer thickness, this step could be repeated for higher purity islets. Finally, the islets were collected and further isolated through a series of six sedimentations (by gravity), with supernatant discarded after 4 minutes following each step. The purified islets were counted under light microscope and then washed 3 times in sterile PBS (1X). Samples were then washed once with RPMI 1640 (+10% HIFBS & 1% Pen/Strep), and then cultured in the same overnight for further use. For human islets, cells were purchased and obtained from ProdoLabs, in line with their rules for ethical sample procurement.

Just before encapsulation, the cultured islets were centrifuged for 1 minute at 1,400 rpm and then washed 3 times with Ca-free KREBS-Henseleit (KH) Buffer (25mM HEPES, 1.2mM $MgSO_4 \times 7H_2O$, 4.7mM KCl, 135mM NaCl, and 1.2mM KH_2PO_4, pH 7.4). Afterwards, islets were centrifuged and all supernatant aspirated. The resulted islet pellet was resuspended in 2% w/v alginate solution (SLG20, in Normal Saline) with or without crystals for an islet density of 1,000 rat islets/ml alginate solution. For human islet preparations, cells were cultured as instructed by the vendor, and 3,000 were suspended per 1 mL alginate solution, with delivery of 2/3 of the total/mouse. Spheres were formed using $BaCl_2$ gelling solution and their sizes controlled as described above. Encapsulated islets were then immediately collected and washed six times with each: HEPES buffer and normal saline, prior to transplantation. Due to variable islets size (50 – 400 μm), with some islet loss during encapsulation, total islet numbers were recounted following encapsulation and converted into islet equivalents (IE) as previously published[62]. For SC delivery, the capsules were placed in 2 separate but elongated subcutaneous (SC) locations, one on each side of the animal (Supplementary Fig. 18). Injection pockets were elongated by tunneling away from the needle stick site and injecting capsules continuously as the needle was slowly withdrawn.

Implantation/Transplantation surgeries

All animal surgeries and protocols were carried out in complete compliance with all relevant ethical regulations, as approved by the MIT Committee on Animal Care, (IACUC). In addition, all surgical procedures as well as the post-operative care were supervised by the veterinary staff of MIT Division of Comparative Medicine. Implant and transplant procedures were carried out as previously described[10,12]. Namely, immune-competent 6–8 week old, male STZ-induced diabetic or non-diabetic C57BL/6 mice (Jackson Laboratory, Bar Harbor, ME) were anesthetized with 3% isoflurane, and then their abdomens (or mid-backs) shaved and sterilized using betadine and isopropanol. All mice received 0.05 mg/kg buprenorphine SC as a pre-surgical analgesic, plus 0.3 ml 0.9% NaCl (to prevent dehydration). Injections using 18-gauge needles were carried out for spheres or a 0.5 cm incision was made along the mid-back for discs for SC implantation. For intraperitoneal (IP) implants, a 0.5–1.0 cm incision was used along the abdomen midline and the peritoneal wall following exposure by blunt dissection. Spheres (either with or without islets) were loaded into sterile pipette tip/needles for injection or PDMS discs (5 mm diameter and 2.2 mm thickness prepared following curing for 10 hours at 45°C of the SYLGARD 184 kit with ratio of 9:1 for elastomer base:curing agent respectively, see Supplementary Fig. 19a) were placed for implantation into the peritoneal space. Then the peritoneal wall was closed with 5–0 polydioxanone (PDS II) bioabsorbable sutures. When appropriate, skin (for both IP and SC methods) was closed with wound clips and tissue glue.

For procedures in non-human primates (NHPs), buprenorphine (0.01–0.03 mg/kg) was preoperatively administered as an analgesic. NHPs were then sedated by intramuscular (IM) ketamine (10 mg/kg) injection, with possible addition of midazolam by vet staff if needed. Animals were kept on circulating warm water-based blankets and covered during the entire procedure for body temperature maintenance. Both SLG20 0.5 or 1.5 mm diameter spheres either no drug or drug-loaded were implanted IP by minimally invasive laparoscopic surgery, or injected SC into the dorsa and flanks of 4–6 kilogram, ~3–5 year old, Cynomolgus Macaques NHPs with 12 and 18 gauge sterile stainless steel needles custom-manufactured (Harvard Apparatus), as previously described[10,12]. Tangentially, the needles were inserted and ~1–2 cm were tunneled away from the initial injection site, to separate the wound field from that of eventual material response. Spheres were injected into four total spots (for subsequent retrievals at time points specified below) with spheres either 0.5 or 1.5 mm in diameter, depending on the animal.

In all cases, experimental endpoints were chosen in order to balance initial goals of characterizing drug effects and therapeutic efficacy with later demonstrating remaining crystalline drug reservoirs over longer periods of time.

Blood glucose monitoring

C57BL/6 mice were treated with streptozotocin (STZ) by the vendor (Jackson Laboratory, Bar Harbor, ME) prior to shipment to MIT to produce diabetic mice. Once received, blood glucose levels (BGs) of all mice were retested to confirm diabetic state prior to transplantation. Only mice with non-fasted BGs > 300 mg/dL for two consecutive days were used.

BGs were measured twice a week after transplantation with capsules (with or without co-encapsulated drug formulation). One blood droplet was collected from the tail vein by lancet and tested using the Clarity Plus commercial glucometer (PN 20212–001, Clarity Diagnostics, LLC., Boca Raton, FL). Tested mice with unfasted BGs < 220 mg/dL were considered cured (normoglycemic). BGs monitoring was continued until sample retrievals.

Retrieval of cells, tissues, and materials

Procedures were carried out as previously described[10,12], and at time points as specified in figures. Briefly, mice were euthanized, and (in some instances) 5 ml of ice cold PBS was injected for IP lavages to collect IP immune cells. An incision was then made along the abdomen and peritoneal wall, and IP lavages were pipetted out into fresh falcon tubes (15 ml, each containing 5 ml RPMI media). Next, a spray bottle with KREBS buffer was used to rinse out all spheres in the abdomen into collection petri dishes. Following ensuring all the spheres were retrieved (manually if need be; e.g. if fibrosed directly to IP tissues), samples were transferred into conical tubes (50 ml) on ice for downstream imaging and processing. Fibrosed IP capsules/tissues were also excised for FACS and expression studies. For SC samples, wide incisions were made in the skin for careful isolation of materials for post-retrieval analyses.

For NHP IP and SC retrievals, animal preparation for live excision procedures was carried out similar to times of implantation (described above). Then, biopsy punches (8-mm) were used to both sample the skin and SC space at 2, 4 weeks and 6 months retrieval time points. Following the retrieval, sites were closed with 3–0 nylon sutures and tissue glue. For IP retrievals, minimally invasive laparoscopic surgery was also used (similar to implant procedures).

Imaging of the retrieved capsules

Phase contrast and brightfield imaging of retrieved materials was carried out as previously described[10–12]. Samples were washed with KREBS buffer and transferred into petri dishes (35 mm) for imaging using an EVOS microscope (Xl, Advanced Microscopy Group) for both phase contrast and brightfield imaging.

Live/Dead islet staining

Carried out as previously described[12]. A LIVE/DEAD Viability/Cytotoxicity kit (CA# L-3224, Life Technologies, Carlsbad, CA) was used as specified by the manufacturer to assess islets viability post-encapsulation with and without co-encapsulated drug formulations.

Confocal immunofluorescence

Immunofluorescence imaging was carried out as previously described[10–12], and used to determine immune populations and fibrotic deposition on implant surfaces. Implants were retrieved from mice as described above and fixed overnight at 4°C with 4% paraformaldehyde. Afterwards, samples were washed 2 times with KREBS, permeabilized for 30 min using 0.1% Triton (X100), and then blocked for 60 min with 1% bovine serum albumin (BSA). Next, the samples were stained for 60 min with a cocktail consisting of DAPI (500 nM), marker probes (1:200 dilution in 1% BSA solution) as noted in displayed Figures (antibodies listed under FACS analysis). Following staining, samples were washed 3 times with 0.1% Tween20 solution and kept in 50% glycerol. Samples imaged in glass bottom plates using a confocal microscope (LSM700, Carl Zeiss Microscopy, Jena Germany).

Histological processing

Retrieved samples were fixed overnight with 4% paraformaldehyde, at 4°C. Tissue-embedded samples were then moved to 70% ethanol, while samples of free alginate spheres were moved directly to saline. Samples were then processed for paraffin embedding, sectioning and staining according to standard histological (Masson's Trichrome or H&E).

qPCR analysis

As previously described[10], RNA was isolated from samples snap-frozen in liquid nitrogen immediately following excision, using the TRIzol protocol (Invitrogen, Carlsbad, CA). Given thorough sample homogenization, displayed gene expression signatures are representative of host response on and/or around retrieved implants. All samples were normalized by loading 1 μg total RNA in all cases for reverse transcription using the High Capacity cDNA Reverse Transcription kit (Catalog number:4368814; Applied Biosystems, Foster City, CA). cDNA (1:20 dilution) was amplified by qPCR with the following primers Mouse α-SMactin (5'-CGCTTCCGCTGCCCAGAGACT-3'; reverse: 5'-TATAGGTGGTTTCGTGGATGCCCGCT-3'), Rat Pdx1 (5'-CTCTCGTGCCATGTGAACC-3'; reverse: 5'-TTCTCTAAATTGGTCCCAGGAA-3'), Rat Cd68 (5'-GCCACAGTACAGTCTACCTTA-3'; reverse: 5'-AGAGATGAATTCTGCGCTGA-3'), Rat α-SMactin (5'-CGCTTCCGCTGCCCGGAGACC-3'; reverse: 5'-TATAGGTGGTTTCGTGGATGCCCGCC-3'), and Rat TNFalpha (5'-CACGCTCTTCTGTCTACTGAACTTC-3'; reverse: 5'-GAGTGTGAGGGTCTGGGCCATG-3') primers were designed with Primer Express (Applied Biosystems, Carlsbad, CA, USA) and evaluated with LaserGene (DNAStar, Madison, WI, USA) to ensure species rat (encapsulated islet) or mouse (host)-specificity. They were also normalized to either mouse (5'-GCTTCTTTGCAGCTCCTTCGTT-3'; reverse: 5'-CGGAGCCGTTGTCGACGACC-3') or rat (5'-ACCTTCTTGCAGCTCCTCCGTC-3'; reverse: 5'-CGGAGCCGTTGTCGACGACG-3') Beta-actin, respectively. Samples were incubated for 10 min at 95°C followed by 40 cycles of 95°C for 15 sec and 60°C for 60 sec in a Roche 480 LightCycler. Results were analyzed using the comparative C_T ($\Delta\Delta C_T$) method and are presented as relative RNA levels, to controls as specified in figure legends, after normalization to β-actin.

FACS analysis

As previously described[10], single-cell suspensions of freshly excised tissues and/or capsules were prepared using a gentle MACS Dissociator (Miltenyi Biotec, Auburn, CA). Sample suspensions were prepared in passive PEB dissociation buffer and passed through 70 μm filters (Catalog number:22363548, Fisher Scientific, Pittsburgh, PA) to remove debris. This procedure yielded the majority of cells adhered to implant surfaces (>90%). All tissue-derived samples were also subjected to red blood cell lysis with 5 ml of 1X RBC lysis buffer (Catalog number:00–4333, eBioscience, San Diego, CA, USA) for 5 min at 4°C, with termination through the addition of 20 ml sterile PBS (1X). Remaining cells were centrifuged (300–400 g at 4°C) and resuspended in 50 μl of eBioscience Staining Buffer (Catalog number:00–4222) for staining in the dark for 25 min at 4°C. Stains included monoclonal antibodies for CD11b (1 μl (0.2 μg) per sample; or CD11b-Alexa-488, Clone M1/70, Catalog number:101217, BioLegend), Ly-6G (Gr-1) (1 μl (0.5 μg) per sample; Ly-6G-Alexa-647, Clone RB6–8C5, Catalog number:108418, BioLegend), and CD68 (1 μl (0.5 μg) per sample; CD68-Alexa647, Clone FA-11, Catalog number:11–5931, BioLegend). 2 ml of stain buffer (Catalog number:00–4222, eBioscience) was then used for 3 consecutive wash steps involving centrifugation for 5 min (400–500 g at 4°C), with supernatants aspirating in-between. Following all washes, samples were resuspended in 500 μl of Flow Cytometry Staining Buffer and run through a 40 μm filter (Catalog number:22363547, Fisher Scientific) for eventual FACS analysis using a BD LSRII or Fortessa (BD Biosciences, San Jose, CA, USA). Unstained, single antibody, and IgG (labled with either Alexa-488 or Alexa-647, BioLegend) controls were also used. For NHP cell staining, anti-human CD68 Alexa Fluor-647-conjugated antibody (Clone KP1, Catalog number:sc-20060, Santa Cruz, Dallas, TX) was used with the BioLegend (anti-mouse/human) CD11b-AF488 antibody (mentioned above).

NanoString analysis

RNAs for mock (saline) controls, or for various drug-loaded 0.5 mm diameter alginate sphere-bearing mice (n=5/group) were isolated from described tissue samples, at various time points post-implantation. They were then quantified, diluted to the appropriate concentration-100 ng/μl, with 5 μl of each sample processed according to manufacturer protocols for analysis with our customized multiplexed gene panels. NHP RNAs collected from samples retrieved over multiple months following implantation of crystal-formulated GW2580 were also analyzed on a separate multiplexed primate gene expression array. Expression levels were obtained following nCounter (NanoString Technologies Inc., Seattle, WA) quantification, with samples analyzed using nSolver analysis software (NanoString Technologies Inc., Seattle, WA). Housekeeping genes: Cltc, Bact, Hprt1, and Tubb5were used to normalize, and data was log-transformed.

LCMS and plasma samples

For this analysis we have used LC pumps of Agilent 1290 Infinity Binary pumps with CTC Pal autosampler and MS of Sciex API6500 triple quad. Samples were stored at −80°C till analysis. An extraction method, namely protein precipitation was applied on the samples with a 10 μl sample processing extraction volume. For example, for GW2580 plasma concentration analysis, the following step-by-step sample extraction procedure was followed: 1. 10 μl of calibration standards and quality controls, blanks, and samples were aliquoted into a 96-well plate. 2. 60 μl of IS-SS (internal standard) (100 ng/ml QNZ, carbutamide, chrysin, carbamazepine, glafenine, dexamethasone, glyburide, and d4AEA in ACN) were added to all samples except for double blanks, while 60 μl of ACN was then added to double blanks. 3. The plate was covered and samples mixed, followed by centrifugation for 5 minutes at ~3000 rpm at 4°C. 4. By using a liquid handler, 50 μl of the supernatant was then transferred to a clean plate. 5. Samples were diluted with 100 μl of MilliQ water, and the plate was once again covered and mixed for about a minute prior to sample injection onto the LC-MS/MS at 1.00–2,500 ng/ml. LC conditions: A C18 column (50 × 2.1 mm, 1.7 μm) of Waters BEH was used and the run temperature was at 50°C. Both mobile phase A (95.0:5.0:0.1 for Water:ACN:FA (1.2 min)) and mobile phase B

(50.0:50.0:0.1 for Methanol:ACN:FA (1.3 min)) were used with 0.8 ml/min as a flow rate and 2 μl as an injection volume. MS Conditions: MS/MS: API-6500, with electrospray ionization method: positive ion, resolution: unit and source temperature of 550°C. Transitions (m/z): Compound ID: GW2580 367.0/245.1 Da. Int Std ID: QNZ 357.0/197.1 Da. Data analysis: regression type-linear (1/(x * x)), accepted curve range 0.50–2,500 ng/ml and carryover 0.00%.

Cryogenic SEM (Cryo-SEM)

Images of 0.5 or 1.5 mm capsules loaded with drug crystals where taken using the Zeiss NVision 40 instrument (Carl Zeiss SMT, Inc.) with the field emission SEM and 1–2 kV acceleration voltages. For sample preparation: 20–50 μl of spherical capsules were first transferred to a proper sample stub and then immersed into a slushy nitrogen bath (liquid and solid). Next, samples were placed in a vacuum cryo transfer system (EM VCT100, Leica Microsystems, Inc.) where by controlled specimen sublimation surface water (ice) was removed in a selective manner. For cross-section images, frozen samples were fractured using a sharp blade. Lastly, prior to imaging both fractured and unfractured spheres were coated with a thin layer of Pt/Pd with a sputter machine..

Continuous glucose monitors (CGMs) coating

Enlite sensor (2nd generation) were coated with PI polymer with drug (i.e. GW2580 or Dexamethasone) at 10% w/w or without, by painting the sensor tip using 29G needle to form a thin uniform layer. Crystals of small size crystals starting from 200 nm up to few microns were used for this application and mixed well with the PI before applying onto the sensor tip. Coated sensors were incubated for 24h at 40ºC for each coated side for full PI curing and solidifying. All sensors were sterilized under UV prior to implantation.

IVIS imaging

Subcutaneous evaluation of CGM inflammatory response was performed as described in Bratlie et al[63]. Each CGM (untreated and treated) was subcutaneously inserted into bilateral sites on the mid-back of female SKH1 mice, ~0.8 cm paramedian to the midline, as previously described[64]. Six days prior to SC insertion, mouse food was changed to special pellets with low fluorescence background (alfalfa-free), and 100 μl of Prosense 750 was injected IP 16–24 hours prior to the imaging time.. Whole body IVIS imaging was then performed, utilizing equivalent regions of interest (ROIs) for quantification of implant groups. Representative inflammation responses (from n = 5 mice in all cases) were shown in displayed images, along with quantification bar graphs (data: mean +/− SEM) with (non-implant) background being subtracted.

CGM in vitro & in vivo functional testing

The *in vitro* glucose-sensing assay was performed with solutions at different glucose concentrations, as previously described[64]. Briefly, the solution was spiked every 15 minutes with a concentrated amount of glucose to bring the solution higher in 20 mg/dL increments. The signal from two sensors in each case (ie., non-coated vs. coated) was plotted as signal versus time, normalized, and graphed.

For *in vivo* functional testing of the sensors, SKH1 mice were anesthetized as previously described[64]. Drug coated and control Medtronic MiniMed EnLite glucose sensors were inserted subcutaneously. Few minutes later sensor hydration period was completed, then iPro2 recording unit was plugged in for data recording.

BGs measurements in mice was started 1–2 hours following sensor insertion in the mice, and the first BG reading was taken. BGs were taken often throughout each day for the first 3 days. BGs from blood droplets collected from the tail vein using a lancet (Medipoint, Inc., Mineola, NY) were measured using the Clarity Plus hand-held monitor (Clarity Plus, PN 20212–001, Clarity Diagnostics, LLC., Boca Raton, FL).

CGM recording data analysis started immediately once recording was completed, and the data was uploaded to the Medtronic CareLink iPro Therapy Management online portal. For calibration, all manually taken BG measurements were used. The Medtronic CareLink iPro online portal then calculated a “Glucose Level” at each time point for the entire recording period, based off of the raw signal trends collected by the iPro recorders.

MSD and MSD drug coated fabrication

The fabrication process for the MSD were done according to the early reported procedure after a slight modification. Shortly the fabrication begins with a silicon wafer as the platform. Onto the bare silicon wafer, a thin layer of polyimide (PI) was spin coated onto the wafer. After curing the polymer base layer, nanoscale layers of gold (Au) and titanium (Ti) were deposited through electron beam deposition onto the polymer layer. Once the metal electrode layers were deposited, standard photolithography techniques were used for the Peano curve design; the wafer was exposed to UV light through a photomask and then selectively etched to produce the pattern. In order to encapsulate the patterned metal traces another PI layer was applied, spin coated on and cured. Then, a layer of aluminum (Al) was deposited to act as a protective layer for the polymer during further etching. This aluminum was then selectively etched and open electrode contact points were produced through photolithography and reactive ion etching. Finally, the MSD devices were detached from the wafer using acetone and wired using Kapton PI tape interconnects. For fabrication MSD drug coated (and it is control) an extra layer for each side surface was applied and coated with PI polymer with drug (i.e. GW2580) at 10% w/w or without, by painting the device side using 29G needle to form a thin uniform layer. Crystals of small size crystals starting from 200 nm up to few microns were used for this application and mixed well with the PI before applying onto the device surface. Coated devices were incubated for 24h at 40ºC for each coated side, plus as needed an extra 24h at the same conditions for full PI curing and solidifying.

MSD in vivo evaluation

All devices were sterilized under UV prior to implantation. Pre-emptive analgesia was administered subcutaneously at the following doses: Buprenex (0.03 mg/kg) and Meloxicam (1.0 mg/kg). All surgical procedures were carried out under isoflurane (2.0%)/Oxygen inhalation. The surgical site was shaven with an electrical clipper and the exposed skin was cleansed with several cycles of betadine scrub followed by isopropanol rinse. All surgeries were performed using aseptic technique. A 1–2 cm incision was made parallel to the femur, and blunt dissection was performed through the vastus lateralis and biceps femoris muscle plains to reveal the sciatic nerve. This nerve was traced down toward the knee until the individual branches (peroneal, sural and tibial) were revealed at the level of popliteal fossa. Tibial nerve was identified as the largest and most central branch. By using micro-dissecting scissors and ultrafine forceps, the tibial nerve was separated from the peroneal and sural nerve branches and carefully was cut as distally as possible as via micro-dissecting scissors thus avoiding the popliteal vessels. The device was sutured securely to the gastrocnemius using four polyprolene sutures. The wires of the device were tunneled subcutaneously up dorsally to reach the incision made at the scalp. Headstages, connected to the end of the wire bundle, were mounted on the skull using dental ceramic. The animals were monitored until consciousness was regained. Post-operative checks were done 14 hours after surgery. Buprenex (0.03 mg/kg) was administered at 8-hour intervals for post-surgical pain management. Meloxicam (1.0 mg/kg) was administered every 24 hours for 48 hours.

Stimulating procedure.—Using the Arduino IDE, we were able to pre-program the desired parameters for functional electrical stimulation and upload it to the rfDuino microcontroller. The system then draws the necessary current out of the low-power coin battery at the set programmed intervals and outputs it to the MSD. The rfDuino is wired to the MSD using thin medical grade stranded stainless steel wire (CoonerWire AS633). The current travels through the MSD and out of the small contact pads where it interfaces with tissue. We sought to determine the therapeutic effects of muscle stimulation using the MSD device for prevention of atrophy during peripheral nerve injury. Five MSD devices of both drug coated and uncoated were implanted along the surface of the gastrocnemius muscles of Lewis rats after resection of the tibial nerves. After surgical implantation, the animals were given 3 days of post-op before initiation of the stimulation regimen. The animals were stimulated with 500 mV, 2 Hz of FES for an hour a day, five days a week for two weeks. Afterwards, the gastrocnemius muscles were collected for histological analysis.

Muscle fiber atrophy quantification.—Axial slices of the gastrocnemius muscle tissue where the device was implanted were analyzed. These slides were stained with H&E and used to quantify muscle fiber area. The slides were scanned and digital images were opened on ImageJ software to measure. The area of muscle fibers can be a good indication of atrophy as muscles tend to decrease in size when not being used. Using the polygon tool and “measure” function – muscle fibers were outlined, measured, and recorded. Multiple images of each slide were taken and at least 200 fibers from each slide were measured. Average muscle fiber areas of the experimental and control groups were calculated and compared to one another.

Statistics and Reproducibility

All line and bar graph data are expressed as mean±SEM, with N=5 mice per time point and per treatment group. The sample sizes where chosen based on previous literature as well as to ensure statistical power in determining data significance. The number of times each experiment was independently repeated is listed in each figure legend. Panels are representative of similar results across experimental repeats. All animals were included except in instances of unforeseen morbidity. Animal cohorts were also randomly selected. Investigators were not blinded to experiments as blinding was not possible for part of the data analysis, especially *in vitro*, due to visual observations of deposited crystalline drug (i.e., having different shading or colors, drug-depending) identifying drug-containing treatment groups. For FACS or qPCR, data were analyzed for statistical significance either by one-way ANOVA with Bonferroni multiple comparison correction or unpaired, two-tailed t-test, unless otherwise indicated, as implemented in GraphPad Prism 7; *:$p<0.05$, **:$p<0.001$, and ***:$p<0.0001$. High-throughput NanoString-based gene expression data was normalized using the geometric means of the positive controls, with background levels established using the means of the negative controls.

Supplementary Material

Refer to Web version on PubMed Central for supplementary material.

ACKNOWLEDGEMENTS

Work was supported by: JDRF-Juvenile Diabetes Research Foundation Grant 17-2007-1063, National Institutes of Health Grants: DE013023, EB000244, CA151884 and EB000351, Leona M. and Harry B. Helmsley Charitable Trust Foundation Grants: 2015PG-T1D063 and 09PG-T1D027, and through a gift from Tayebati Family Foundation. J.C.D. was supported by postdoctoral fellowship from JDRF (Fellowship: 3-PDF-2015-91-A-N). J.O. is supported by the Chicago Diabetes Project and the National Institutes of Health (NIH/NIDDK) R01DK091526. G.C.W. is supported by the National Institutes of Health Diabetes Research Centers Grant P30 DK 36836. D.L.G. is supported by the National Institutes of Health (NIH/NIDDK) UC4 DK104218. We would like to acknowledge the use of resources at Core Facilities (Swanson Biotechnology Center, David H. Koch Institute for Integrative Cancer Research at MIT) and W.M. Keck Biological Imaging Facility for Flow Cytometry, Histology, *in situ* Accelerated Release Microscopy (Wendy C. Salmon, Whitehead Institute), Animal Imaging, and Scanning Electron Microscopy.

REFERENCES

1. Fattahi P, Yang G, Kim G. & Abidian MR A review of organic and inorganic biomaterials for neural interfaces. Advanced materials 26, 1846–1885, 10.1002/adma.201304496 (2014). [PubMed: 24677434]
2. Nichols SP, Koh A, Storm WL, Shin JH & Schoenfisch MH Biocompatible materials for continuous glucose monitoring devices. Chemical reviews 113, 2528–2549, 10.1021/cr300387j (2013). [PubMed: 23387395]
3. Rosen MR, Robinson RB, Brink PR & Cohen IS The road to biological pacing. Nat Rev Cardiol 8, 656–666, 10.1038/nrcardio.2011.120 (2011). [PubMed: 21844918]
4. Farra R. et al. First-in-human testing of a wirelessly controlled drug delivery microchip. Sci Transl Med 4, 122–121, 10.1126/scitranslmed.3003276 (2012).
5. Hubbell JA & Langer R. Translating materials design to the clinic. Nat Mater 12, 963–966, 10.1038/nmat3788 (2013). [PubMed: 24150414]
6. Kearney CJ & Mooney DJ Macroscale delivery systems for molecular and cellular payloads. Nat Mater 12, 1004–1017, 10.1038/nmat3758 (2013). [PubMed: 24150418]
7. Yoo JW, Irvine DJ, Discher DE & Mitragotri S. Bio-inspired, bioengineered and biomimetic drug delivery carriers. Nat Rev Drug Discov 10, 521–535, 10.1038/nrd3499 (2011). [PubMed: 21720407]
8. Kenneth Ward W. A Review of the Foreign-body Response to Subcutaneously-implanted Devices: The Role of Macrophages and Cytokines in Biofouling and Fibrosis. J. Diabetes Sci. Technol. Online 2, 768–777 (2008).
9. Anderson JM, Rodriguez A. & Chang DT Foreign body reaction to biomaterials. Semin Immunol 20, 86–100, 10.1016/j.smim.2007.11.004 (2008). [PubMed: 18162407]

10. Doloff JC et al. Colony stimulating factor-1 receptor is a central component of the foreign body response to biomaterial implants in rodents and non-human primates. Nat Mater 16, 671–680, 10.1038/nmat4866 (2017). [PubMed: 28319612]
11. Vegas AJ et al. Combinatorial hydrogel library enables identification of materials that mitigate the foreign body response in primates. Nat Biotechnol 34, 345–352, 10.1038/nbt.3462 (2016). [PubMed: 26807527]
12. Veiseh O. et al. Size- and shape-dependent foreign body immune response to materials implanted in rodents and non-human primates. Nat Mater 14, 643–651, 10.1038/nmat4290 (2015). [PubMed: 25985456]
13. Rhen T. & Cidlowski JA Antiinflammatory action of glucocorticoids--new mechanisms for old drugs. New England Journal of Medicine 353, 1711 (2005). [PubMed: 16236742]
14. Schneider BL, Schwenter F, Pralong WF & Aebischer P. Prevention of the initial host immuno-inflammatory response determines the long-term survival of encapsulated myoblasts genetically engineered for erythropoietin delivery. Mol Ther 7, 506–514 (2003). [PubMed: 12727114]
15. Zhang WJ et al. HOE 077 reduces fibrotic overgrowth around the barium alginate microcapsules. Transplant Proc 32, 206–209 (2000). [PubMed: 10701026]
16. Attur MG et al. Differential anti-inflammatory effects of immunosuppressive drugs: cyclosporin, rapamycin and FK-506 on inducible nitric oxide synthase, nitric oxide, cyclooxygenase-2 and PGE 2 production. Inflammation Research 49, 20–26 (2000). [PubMed: 10778917]
17. Cannarile MA et al. Colony-stimulating factor 1 receptor (CSF1R) inhibitors in cancer therapy. J Immunother Cancer 5, 53, 10.1186/s40425-017-0257-y (2017). [PubMed: 28716061]
18. Wehling M. Non-steroidal anti-inflammatory drug use in chronic pain conditions with special emphasis on the elderly and patients with relevant comorbidities: management and mitigation of risks and adverse effects. Eur J Clin Pharmacol 70, 1159–1172, 10.1007/s00228-014-1734-6 (2014). [PubMed: 25163793]
19. Srinivasan A. & De Cruz P. Review article: a practical approach to the clinical management of NSAID enteropathy. Scand J Gastroenterol 52, 941–947, 10.1080/00365521.2017.1335769 (2017). [PubMed: 28587496]
20. Lin J. et al. TNFalpha blockade in human diseases: an overview of efficacy and safety. Clin Immunol 126, 13–30, 10.1016/j.clim.2007.08.012 (2008). [PubMed: 17916445]
21. Gyorfi AH, Matei AE & Distler JHW Targeting TGF-beta signaling for the treatment of fibrosis. Matrix Biol, 10.1016/j.matbio.2017.12.016 (2018).
22. Murray PJ & Wynn TA Protective and pathogenic functions of macrophage subsets. Nat Rev Immunol 11, 723–737, 10.1038/nri3073 (2011). [PubMed: 21997792]
23. Dang TT et al. Spatiotemporal effects of a controlled-release anti-inflammatory drug on the cellular dynamics of host response. Biomaterials 32, 4464–4470, 10.1016/j.biomaterials.2011.02.048 (2011). [PubMed: 21429573]
24. Singarayar S, Kistler PM, De Winter C. & Mond H. A comparative study of the action of dexamethasone sodium phosphate and dexamethasone acetate in steroid-eluting pacemaker leads. Pacing Clin Electrophysiol 28, 311–315, 10.1111/j.1540-8159.2005.40055.x (2005). [PubMed: 15826265]
25. Friedl KE Corticosteroid modulation of tissue responses to implanted sensors. Diabetes Technol Ther 6, 898–901, 10.1089/dia.2004.6.898 (2004). [PubMed: 15684645]
26. Gilligan BC et al. Feasibility of continuous long-term glucose monitoring from a subcutaneous glucose sensor in humans. Diabetes Technol Ther 6, 378–386, 10.1089/152091504774198089 (2004). [PubMed: 15198842]
27. Vacanti NM et al. Localized delivery of dexamethasone from electrospun fibers reduces the foreign body response. Biomacromolecules 13, 3031–3038, 10.1021/bm300520u (2012). [PubMed: 22920794]
28. Weldon CB et al. Electrospun drug-eluting sutures for local anesthesia. J Control Release 161, 903–909, 10.1016/j.jconrel.2012.05.021 (2012). [PubMed: 22609349]
29. Ricci M. et al. Ketoprofen controlled release from composite microcapsules for cell encapsulation: effect on post-transplant acute inflammation. Journal of Controlled Release 107, 395–407 (2005). [PubMed: 16129507]

30. Einmahl S. et al. Concomitant and controlled release of dexamethasone and 5-fluorouracil from poly (ortho ester). International Journal of Pharmaceutics 185, 189–198 (1999). [PubMed: 10460914]

31. Siepmann J, Siegel RA & Rathbone MJ in Advances in delivery science and technology 1 online resource (xiii, 592 p (Springer,, New York, 2012).

32. Bain CC et al. Constant replenishment from circulating monocytes maintains the macrophage pool in the intestine of adult mice. Nat Immunol 15, 929–937, 10.1038/ni.2967 (2014). [PubMed: 25151491]

33. Mosser DM & Edwards JP Exploring the full spectrum of macrophage activation. Nat Rev Immunol 8, 958–969, 10.1038/nri2448 (2008). [PubMed: 19029990]

34. Singh MN, Hemant KS, Ram M. & Shivakumar HG Microencapsulation: A promising technique for controlled drug delivery. Res Pharm Sci 5, 65–77 (2010). [PubMed: 21589795]

35. Cobelli N, Scharf B, Crisi GM, Hardin J. & Santambrogio L. Mediators of the inflammatory response to joint replacement devices. Nat Rev Rheumatol 7, 600–608, 10.1038/nrrheum.2011.128 (2011). [PubMed: 21894210]

36. Desbois S, Seabrook SA & Newman J. Some practical guidelines for UV imaging in the protein crystallization laboratory. Acta Crystallogr Sect F Struct Biol Cryst Commun 69, 201–208, 10.1107/S1744309112048634 (2013).

37. Niedzialkowska E. et al. Protein purification and crystallization artifacts: The tale usually not told. Protein Sci 25, 720–733, 10.1002/pro.2861 (2016). [PubMed: 26660914]

38. Farah S, Khan W. & Domb AJ Crystalline coating of rapamycin onto a stent: process development and characterization. Int J Pharm 445, 20–28, 10.1016/j.ijpharm.2013.01.053 (2013). [PubMed: 23380625]

39. Levy Y, Khan W, Farah S. & Domb AJ Surface crystallization of rapamycin on stents using a temperature induced process. Langmuir 28, 6207–6210, 10.1021/la300364y (2012). [PubMed: 22462404]

40. Puhl S, Meinel L. & Germershaus O. Recent advances in crystalline and amorphous particulate protein formulations for controlled delivery. Asian J Pharm Sci 11, 469–477, 10.1016/j.ajps.2016.06.003 (2016).

41. Yaghmur A, Rappolt M, Ostergaard J, Larsen C. & Larsen SW Characterization of bupivacaine-loaded formulations based on liquid crystalline phases and microemulsions: the effect of lipid composition. Langmuir 28, 2881–2889, 10.1021/la203577v (2012). [PubMed: 22247936]

42. Farah S. Protective Layer Development for Enhancing Stability and Drug-Delivery Capabilities of DES Surface-Crystallized Coatings. ACS Appl Mater Interfaces 10, 9010–9022, 10.1021/acsami.7b18733 (2018). [PubMed: 29436817]

43. Kalepu S. & Nekkanti V. Insoluble drug delivery strategies: review of recent advances and business prospects. Acta Pharm Sin B 5, 442–453, 10.1016/j.apsb.2015.07.003 (2015). [PubMed: 26579474]

44. Dang TT et al. Enhanced function of immuno-isolated islets in diabetes therapy by co-encapsulation with an anti-inflammatory drug. Biomaterials 34, 5792–5801, 10.1016/j.biomaterials.2013.04.016 (2013). [PubMed: 23660251]

45. Wu P. & Grainger DW Drug/device combinations for local drug therapies and infection prophylaxis. Biomaterials 27, 2450–2467, 10.1016/j.biomaterials.2005.11.031 (2006). [PubMed: 16337266]

46. Murray PJ et al. Macrophage activation and polarization: nomenclature and experimental guidelines. Immunity 41, 14–20, 10.1016/j.immuni.2014.06.008 (2014). [PubMed: 25035950]

47. Chadha R, Arora P, Saini A. & Jain DS Solvated crystalline forms of nevirapine: thermoanalytical and spectroscopic studies. AAPS PharmSciTech 11, 1328–1339, 10.1208/s12249-010-9511-z (2010). [PubMed: 20737259]

48. Chadha R, Kuhad A, Arora P. & Kishor S. Characterisation and evaluation of pharmaceutical solvates of Atorvastatin calcium by thermoanalytical and spectroscopic studies. Chem Cent J 6, 114, 10.1186/1752-153X-6-114 (2012). [PubMed: 23039933]

49. Olafson KN, Ketchum MA, Rimer JD & Vekilov PG Mechanisms of hematin crystallization and inhibition by the antimalarial drug chloroquine. Proc Natl Acad Sci U S A 112, 4946–4951, 10.1073/pnas.1501023112 (2015). [PubMed: 25831526]

50. Datta S. & Grant DJ Crystal structures of drugs: advances in determination, prediction and engineering. Nat Rev Drug Discov 3, 42–57, 10.1038/nrd1280 (2004). [PubMed: 14708020]

51. Kempster CJE & Lipson H. A rapid method for assessing the number of molecules in the unit cell of an organic crystal. Acta Crystallographica Section B: Structural Crystallography and Crystal Chemistry 28.12, 3674–3674 (1972).

52. de Groot M, Schuurs TA & van Schilfgaarde R. Causes of limited survival of microencapsulated pancreatic islet grafts. J Surg Res 121, 141–150, 10.1016/j.jss.2004.02.018 (2004). [PubMed: 15313388]

53. Pepper AR et al. A prevascularized subcutaneous device-less site for islet and cellular transplantation. Nat Biotechnol 33, 518–523, 10.1038/nbt.3211 (2015). [PubMed: 25893782]

54. Simeonovic CJ, Dhall DP, Wilson JD & Lafferty KJ A comparative study of transplant sites for endocrine tissue transplantation in the pig. Aust J Exp Biol Med Sci 64 (Pt 1), 37–41 (1986). [PubMed: 3083804]

55. Georgiev A. et al. in High Performance Polymers - Polyimides Based - From Chemistry to Applications (ed Abadie JM) (Intech, 2012).

SUPPLEMENTARY REFERENCES

56. Bruker. SAINT, Bruker-AXS Inc Madison, Wisconsin, USA; 2011.

57. Krause L, Herbst-Irmer R, Sheldrick GM, Stalke D. Comparison of silver and molybdenum microfocus X-ray sources for single-crystal structure determination. J Appl Crystallogr 2015, 48(Pt 1): 3–10. [PubMed: 26089746]

58. Sheldrick GM. SHELXT - integrated space-group and crystal-structure determination. Acta Crystallogr A Found Adv 2015, 71(Pt 1): 3–8. [PubMed: 25537383]

59. Sheldrick GM. Crystal structure refinement with SHELXL. Acta Crystallogr C Struct Chem 2015, 71(Pt 1): 3–8. [PubMed: 25567568]

60. Müller P. Practical suggestions for better crystal structures. Crystallography Reviews 2009, 15(1): 57–83.

61. Lacy PE, Kostianovsky M. Method for the isolation of intact islets of Langerhans from the rat pancreas. Diabetes 1967, 16(1): 35–39. [PubMed: 5333500]

62. Ricordi C, Gray DW, Hering BJ, Kaufman DB, Warnock GL, Kneteman NM, et al. Islet isolation assessment in man and large animals. Acta Diabetol Lat 1990, 27(3): 185–195. [PubMed: 2075782]

63. Bratlie KM et al. Rapid biocompatibility analysis of materials via in vivo fluorescence imaging of mouse models. PLoS One 5, (2010).

64. Xie X. et al. Reduction of measurement noise in a continuous glucose monitor by coating the sensor with a zwitterionic polymer. Nat BME 2, 894–906, 10.1038/s41551-018-0273-3 (2018).

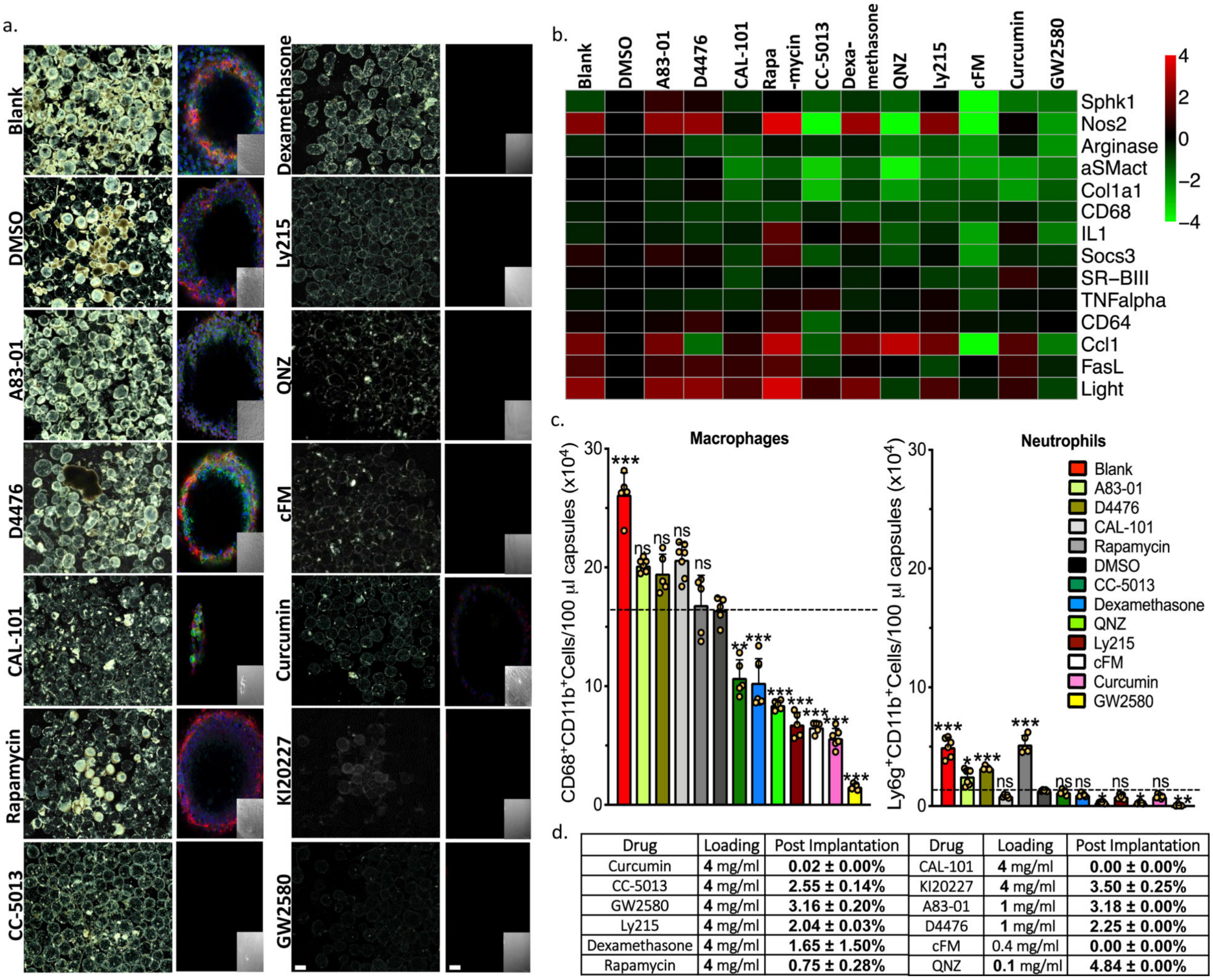

Drug	Loading	Post Implantation	Drug	Loading	Post Implantation
Curcumin	**4** mg/ml	**0.02 ± 0.00%**	CAL-101	**4** mg/ml	**0.00 ± 0.00%**
CC-5013	**4** mg/ml	**2.55 ± 0.14%**	KI20227	**4** mg/ml	**3.50 ± 0.25%**
GW2580	**4** mg/ml	**3.16 ± 0.20%**	A83-01	**1** mg/ml	**3.18 ± 0.00%**
Ly215	**4** mg/ml	**2.04 ± 0.03%**	D4476	**1** mg/ml	**2.25 ± 0.00%**
Dexamethasone	**4** mg/ml	**1.65 ± 1.50%**	cFM	0.4 mg/ml	**0.00 ± 0.00%**
Rapamycin	**4** mg/ml	**0.75 ± 0.28%**	QNZ	**0.1** mg/ml	**4.84 ± 0.00%**

Figure 1. Anti-fibrotic drug screen. Testing agents largely targeted to macrophage biology.

a) Phase contrast and confocal images, respectively, of capsules (Blank, DMSO vehicle, or containing amorphous drug, as indicated) retrieved following implantation into the IP space of C57BL/6 mice for two weeks. Phase contrast images showing host FBR immune cell adhesion and fibrosis Confocal microscopy images showing reduced or no fibrotic overgrowth on alginate microcapsules (Blue, DAPI nuclear stain; Green:cellular cytoskeleton marker F-actin; and Red:Fibrosis marker αSMactin. Insets:brightfield images of the same fields of view in the main confocal panel). Scale bars, phase contrast:500μm; confocal image:50μm. **b**) Multiplexed NanoString gene expression analysis of macrophage subtyping and Fibrosis markers for RNA isolated from the surface of free-floating Blank (no drug), drug vehicle (DMSO-for amorphous formulations), and amorphous drug loaded microsphere capsules, following a 2-week implantation in C57BL/6 mice. Interestingly, both cFM and GW2580 target CSF1R, and show almost identical gene expression responses. Red:increase in expression; Green:decrease in expression, as compared to vehicle (DMSO)-loaded. **c**) Quantitative FACS analysis of macrophage and neutrophils respectively performed on cells dissociated directly off of alginate spheres. Some drugs significantly reduced macrophage and neutrophils presence. Data:mean±SEM. **d**) Table showing that all compounds, encapsulated in their amorphous form, either ran out or had less than 5% drug remaining after only a 2-week IP implantation in C57BL/6 mice. All bar graph data:mean ±SEM. Statistical analysis:one-way ANOVA plus Bonferroni multiple comparison correction; *:p<0.05; **:p<0.001, and ***:p<0.0001; ns=not significantly different. For all *in vivo* data, N=5 mice/group. All subpanels reflect representative data from *in vivo* experiments repeated 3 times.

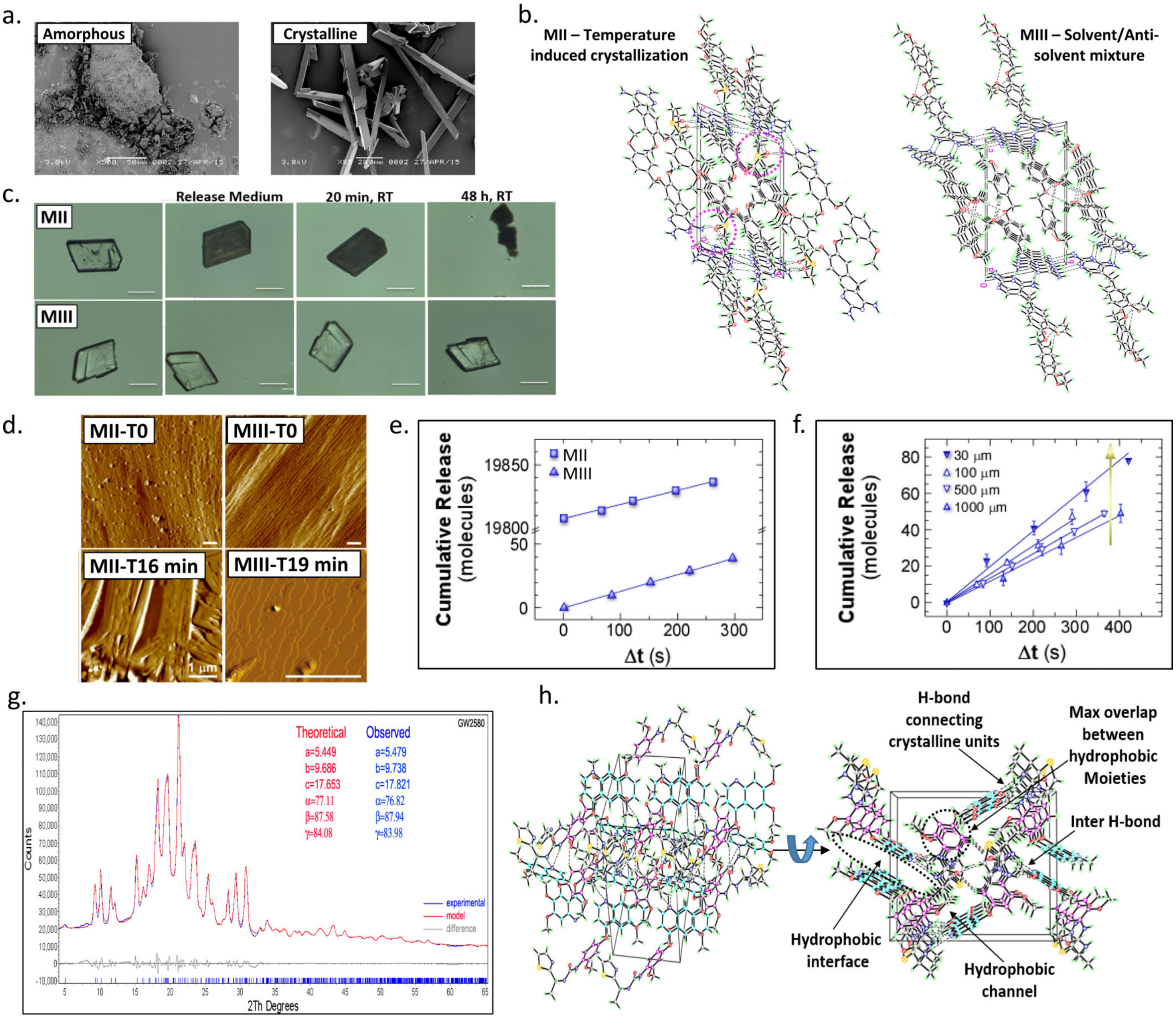

Figure 2. Crystal development and characterization. In depth comparison of crystal forms derived from different crystallization methods.

a) Representative SEM images of fine amorphous and large crystals of the CSF1R inhibitor GW2580 (See Supplementary Fig. 4b). **b**) Two representative examples of the 3D packing pattern inside the GW2580 crystals developed by two crystallization methods: MII versus MIII as revealed by SXRD, exhibiting solvent molecule inclusion/involvement inside the crystalline units (MII) vs. solvent-free crystals (MIII). **c**) Microscope images showing the first contact of GW2580 crystals with aqueous medium (PBS). MII crystals turn opaque-to-black due to fast release attributed to solvent-facilitated collapse, while MIII crystals exhibited slow surface release over the same period. Scale bar=100μm. **d**) Time-resolved *in situ* AFM showing real-time release from GW2580 crystal surfaces in a physiologically relevant environment (PBS, 37ºC). MII and MIII crystals were monitored at t=0 (open to air) and t=16 min or 19 min, respectively (in solution). Scale bars=1μm. **e**) Cumulative molecules released from the surface of GW2580 crystals found by *in situ* AFM:MII vs. MIII (same size). Time axis:$\Delta t = t - t_0$ where t is the time of image collection and t_0 is the elapsed time between addition of buffer and heating to 37°C and the first dissolution measurement (See Supplementary Fig. 5). Error bars are smaller than the symbol size. **f**) Cumulative molecules released from MIII crystals of different size, where $t_0 \approx 300$ s across all independent *in situ* AFM experiments. All line graphs data:mean±SEM. **g**) PXRD polymorph analysis (theoretical vs. measured) of CSF1R inhibitor GW2580. **h**) Two representative SXRD crystal structures (different rotations of Ki20227) showing interaction (hydrophobic and hydrogen bonds) between the drug molecule’s moieties inside the crystalline units as well as hydrogen bonds (semi-crosslinkers) between the repeating units. All subpanels reflect representative data from *in vitro* experimental analyses repeated 3 times.

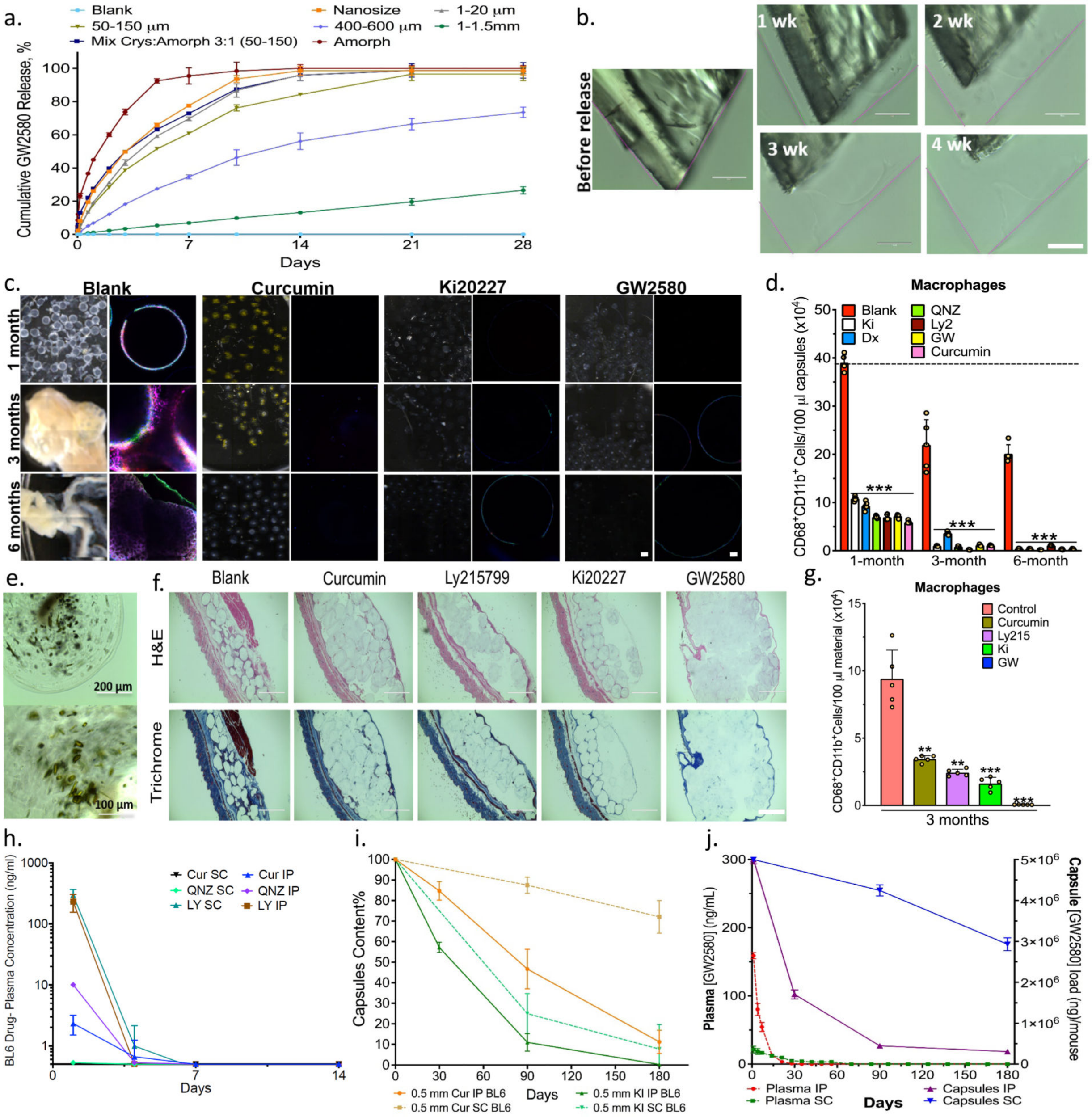

Figure 3. *In vitro* release and *in vivo* anti-fibrotic efficacy.

Agents tested in alginate spheres both *in vitro* and in C57BL/6 mice. **a**) *In vitro* GW2580 (GW) release under accelerated conditions (37ºC, PBS+0.1% SDS) encapsulated within 2000μm alginate capsules. Release from crystalline formulations tuned by varying crystal size and amorphous-to-crystalline ratio (as specified), Mean+/−SD. **b**) Surface erosion of GW2580 large crystal over 1-to-4 weeks; original dimensions shown with pink lines. Scale bar=100μm. **c**) Phase contrast and confocal images for retrieved capsules after 1, 3, and 6-month IP implantations. Phase contrast images showing host FBR, observed as yellowish-white plaque on otherwise translucent alginate microspheres. Crystalline formulations encapsulated in 500μm alginate spheres showed significant long-term anti-fibrotic efficacy. Note:drug crystals have a colored appearance, making capsules more opaque (See

Supplementary Fig. 10c). Confocal images showing reduced or no fibrotic overgrowth with drug crystals (Blue, DAPI nuclear stain; Green:Macrophage CD68; and Red:Fibrosis marker αSMactin). Scale bars, phase contrast:500μm; confocal image:50μm. **d**) FACS analysis performed on cells dissociated from retrieved spheres after 1, 3, and 6 months post-IP implantation. **e**) Images of retrieved capsules containing crystalline curcumin after 6 months post-IP implantation. **f**) H&E and Masson's Trichrome stained histologic sections of 3-month subcutaneous (SC) implants (+tissue) showing reduced fibrosis with crystalline drugs, vs. blank controls (Scale bar=1000μm; 4X). **g**) Flow analysis for macrophages dissociated from spheres, (100μl material in all cases) 3 months following SC implantation. **h**) Plasma drug concentrations from separate crystalline-drug formulations SC or IP implantations (Cur:curcumin; LY:Ly2157299; and QNZ). Though shown to 14 days, all drugs were monitored and remained below detection limits up to 180 days. **i**) HPLC-determined capsule drug content after 1, 3, and 6-months (SC&IP) for crystalline curcumin and Ki20227. **j**) LCMS determination of GW2580 levels in plasma (Left-y-axis) vs. in capsules (Right-y-axis) following SC or IP implantation. *In vitro*, N=3 samples/group. All line and bar graph data:mean±SEM. Statistical analysis:one-way ANOVA plus Bonferroni multiple comparison correction; **:p<0.001, and ***:p<0.0001. *In vivo* studies, N=5 mice/group. All subpanels reflect representative data from *in vitro* or *in vivo* experimental analyses repeated 3-times in each case.

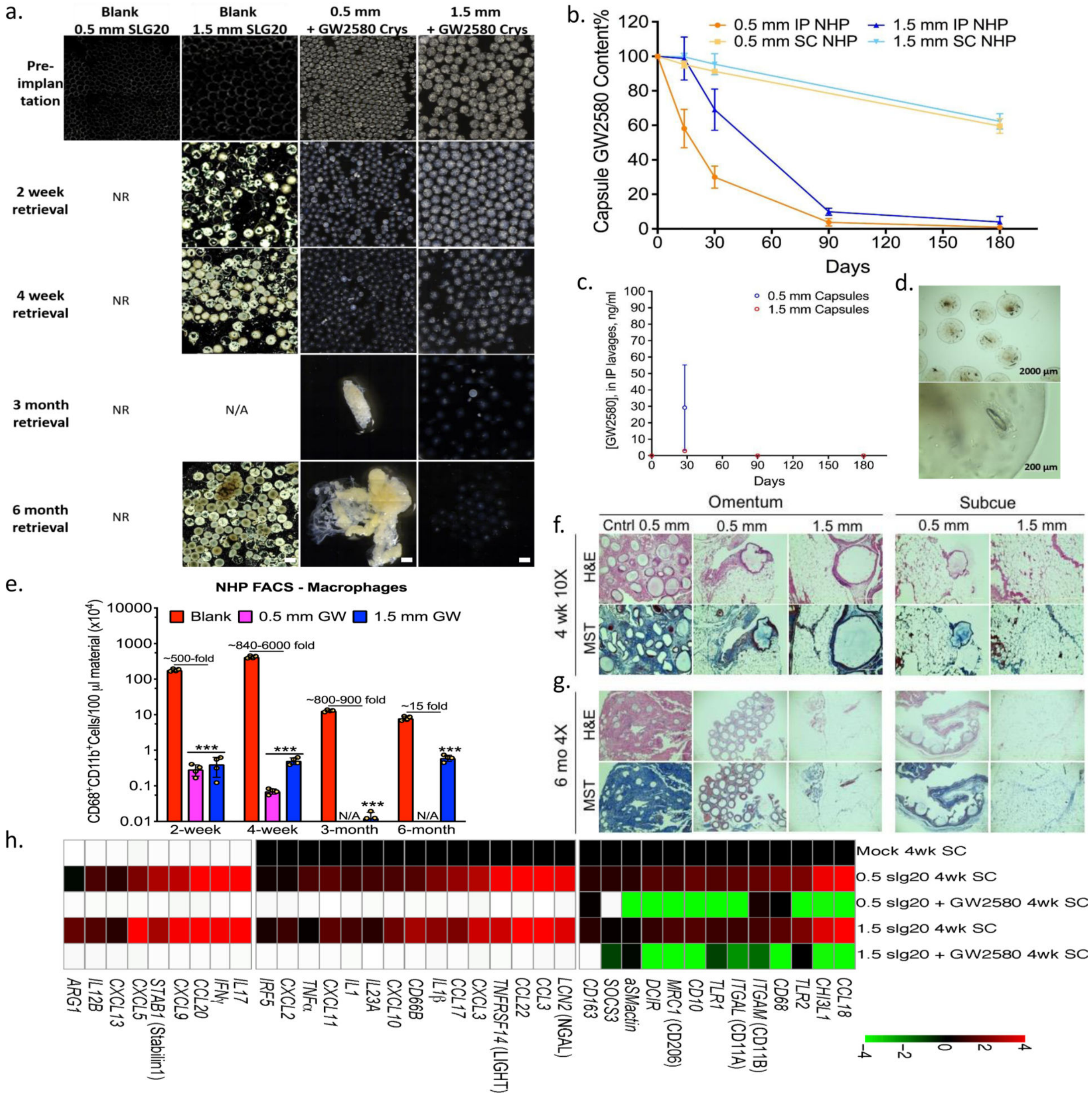

Figure 4. Long-term anti-fibrotic efficacy in non-human primates.

Crystalline GW2580 was tested in alginate spheres across different implant sites. **a**) Phase contrast images showing host FBR against 0.5 and 1.5 mm diameter alginate spheres encapsulating crystalline CSF1R inhibitor GW2580, after 2 and 4-week as well as 3 and 6-month intraperitoneal (IP) implantations in non-human primates (NHP); N=2/group. See Supplementary Fig. 12 for a full IP and SC implant panel over time. Note: drug crystals have colored appearance, making drug loaded-alginate capsules more opaque/white. NR=not-retrievable, N/A=not-available. Scale bars=1500µm. **b**) Drug extraction analysis (HPLC) revealed significant crystals quantities left inside retrieved capsules (up to 8% or 68% of initial loading for IP or SC capsules, respectively). **c**) Lavage GW2580 concentrations from the IP space surrounding 0.5 mm and 1.5 mm implanted capsules. **d**) Microscopy images showing retrieved 1.5 mm capsules after 6 months from IP space. Crystals were found to release in a gradual manner leaving hollow spaces. **e**) Quantitative FACS analysis of cells dissociated from alginate spheres, retrieved after various post-IP implantation times, as specified, vs. 1.5 mm blank SLG20 capsules. Macrophage presence is reduced with drug as compared to empty (control) spheres (log base 10 scale). H&E and Masson's Trichrome stained histological sections of excised IP omentum or SC tissue 4 weeks (**f**) and 6 months (**g**) post-implant showing reduced fibrosis in various crystalline drug (GW2580) groups, vs. blank 0.5 mm control spheres (Scale bars=400μm (10X) or 1000 μm (4X), respectively). **h**) NanoString analysis of 4-week implanted SC tissues for immune markers and cytokines, as compared to mock (saline-injected) controls. White-within two standard deviations of assay's mean background. All bar or line graph data:mean±SEM. Statistical analysis:one-way ANOVA plus Bonferroni multiple comparison correction; ***:$p<0.0001$. N=4 samples/group. All subpanels reflect representative data from *in vivo* experimental analyses repeated twice.

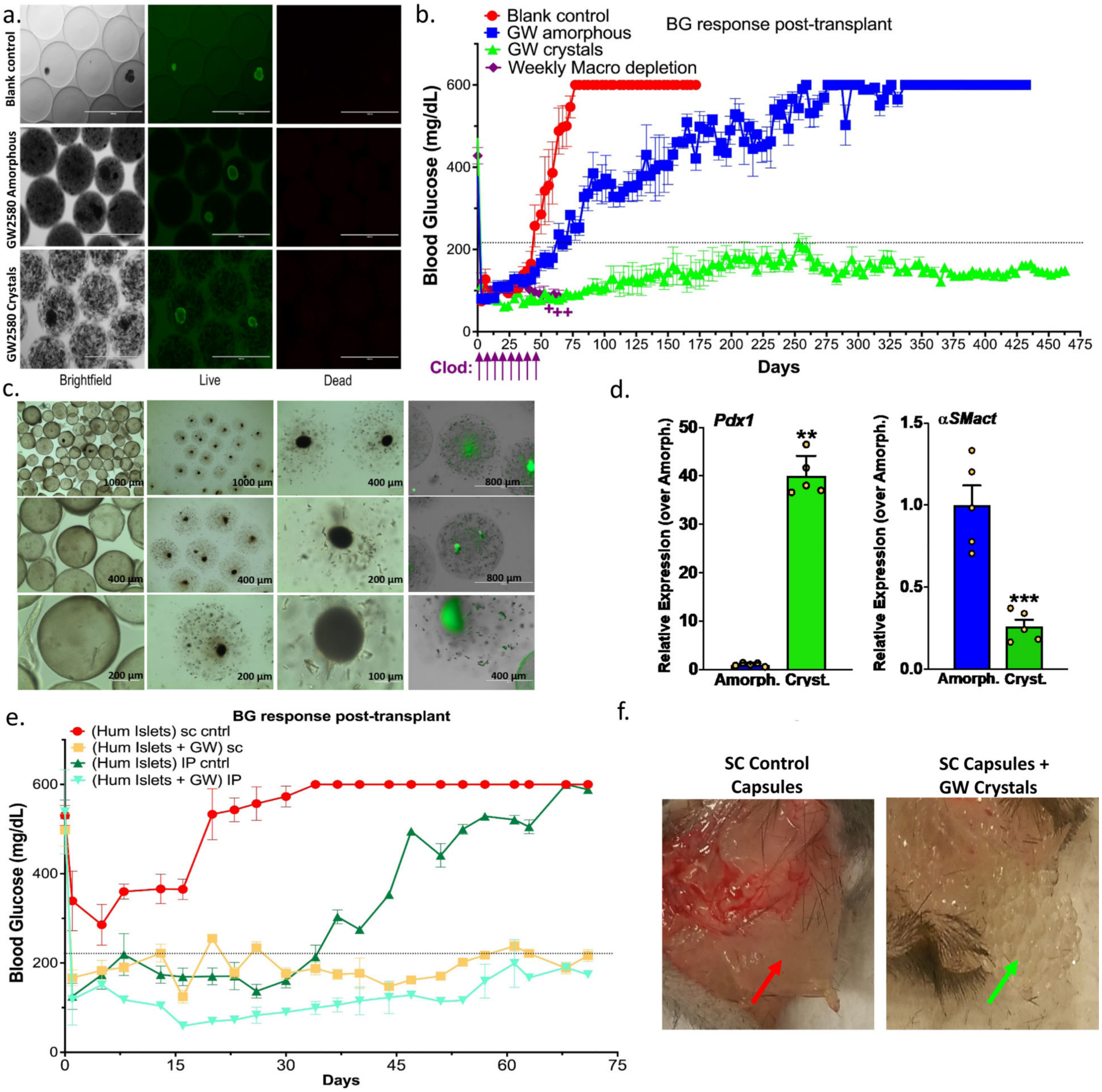

Figure 5. Long-term glycemic control with crystalline GW2580.

Drug was co-encapsulated with islets (rat or human) and transplanted into STZ-C57BL/6 diabetic mice. **a**) Live/dead staining confirming viability of rat islet cells with both amorphous and crystalline GW2580 prepared in ~500–600µm alginate capsules; Scale bar=1000µm. Image rows: same field of view, focus and magnification. **b**) Blood glucose curves showing significantly prolonged normoglycemic maintenance with crystalline GW2580 (GW, green), over blank (no drug, red) controls and amorphous-loaded (blue) capsules co-encapsulating 500 IE (islet equivalents) rat islets and transplanted IP. Macrophage-depleting clodrosomes (Clodro, liposomal-clodronate), were administered weekly (purple arrows) as positive control (++:group was terminated due to toxicity). **c**) Brightfield images, capsules after 15 months; amorphous: first column and crystal-loaded

(2nd and 3rd columns). Islets are visible as dark-black circles. In the 4th column both cells and crystals under green (auto) fluorescence. **d**) Rat Pdx1 and host αSMactin expression from capsules retrieved at ~430 or 460 (~1.3 years) days post-transplant, respectively, for amorphous and crystalline GW. **e**) Blood glucose curves showing prolonged normoglycemia for ~500–600μm capsules co-encapsulating 2000 IE (islet equivalents) human islets transplanted in diabetic C57BL/6 mice with GW crystals (gold:SC; teal-blue:IP) vs. without (red:SC; green:IP). Capsules without GW failed after ~32 days in the IP space, and in the SC space did not provide glycemic control. In contrast, capsules with GW crystals provided glycemic control for over 72 days (termination time-point) in both IP and SC. **f**) Photos showing control and GW-loaded capsules retrieved after the 72-day SC transplantation. Control capsules were fully fibrosed forming a solid collagen-encapsulated sack, compared to fibrosis-free crystalline GW-loaded capsules. All line/bar graph data:mean±SEM. Statistical analysis:one-way ANOVA plus Bonferroni multiple comparison correction; **:$p<0.001$, and ***:$p<0.0001$. *In vivo* studies, N=5 mice/group. All subpanels reflect representative data from experimental analyses repeated twice.

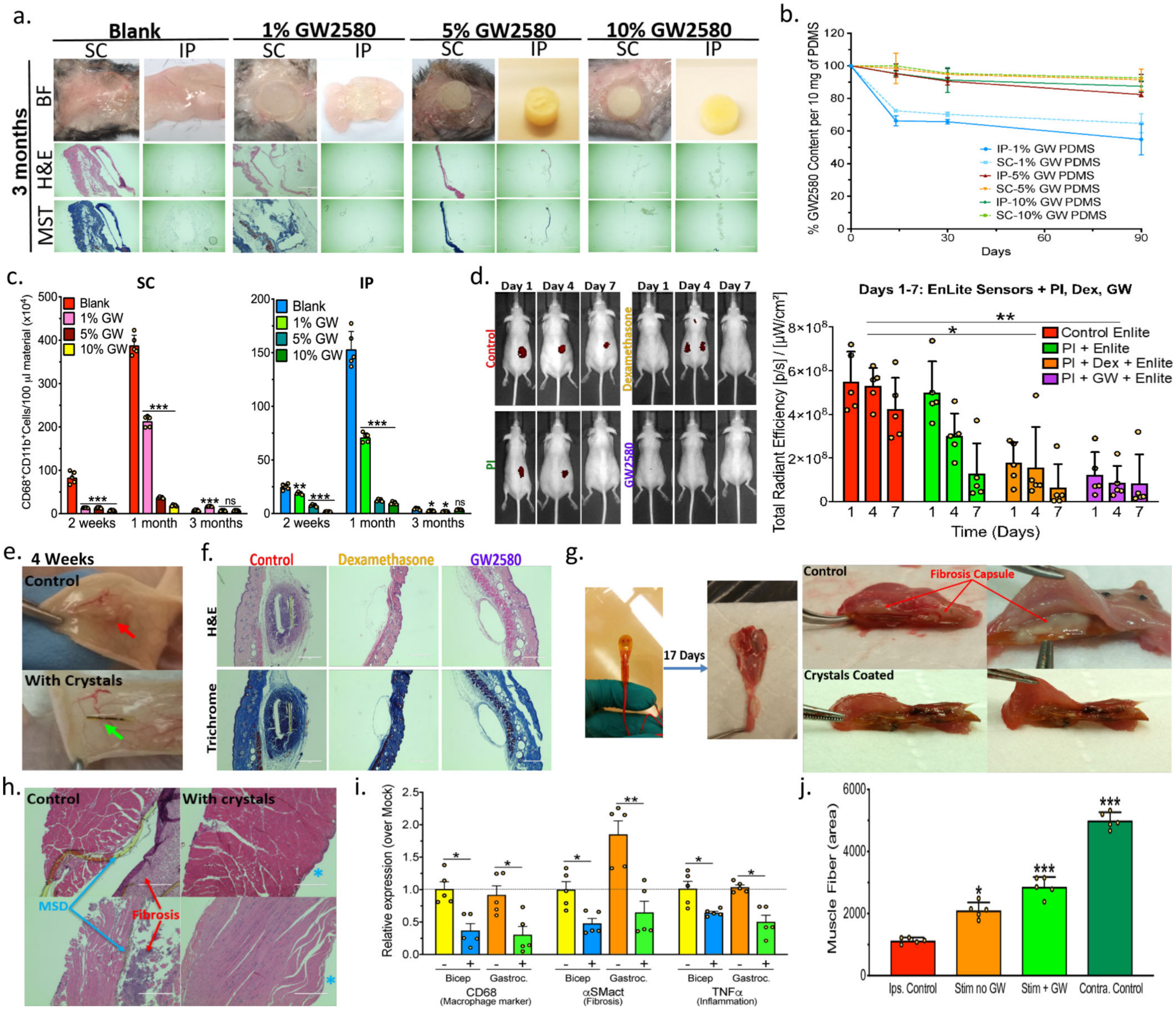

Figure 6. Long-term drug depot effects of GW2580 crystals.

Drug was loaded within cured PDMS discs or surface coatings on multi-component devices. **a**) Brightfield (BF), H&E and Masson's Trichrome histology images of excised 3-month SC and IP tissue+PDMS discs, loaded with 0 (Blank), 1, 5, or 10% crystalline GW2580 (GW), in C57BL/6 mice. Scale bar=1000µm; 4X. (See Supplementary Fig.19). **b**) GW loading% (by-HPLC) following SC or IP 3-month implantation. **c**) Flow analysis for macrophages dissociated from discs 3 months SC and IP post-implantation. **d**) IVIS-measured implant-induced SC inflammation using ProSense at 1, 4, & 7 days post-insertion in SKH1-mice. Native CGMs (control), Polyimide-(PI)-coating alone or with crystalline drug (Dexamethasone-(Dex) or (GW)) were used. **e**) Photos showing crystalline GW-coated CGMs with reduced fibrosis after 4-week SC implantations, vs. controls. **f**) H&E and Masson's Trichrome staining of excised 4-week SC implants, showing reduced fibrosis with crystalline drug (either Dex or GW), as compared to control CGMs (Scale bar=400µm

(10X)). **g**) Retrieved MSDs 17 days after suturing to gastrocnemius muscle (IM implantation) in rats. Cross-section images:thick fibrosis for controls (>500μm) versus no significant fibrosis with crystalline GW. **h**) H&E-stained sections of tissues excised 17 days post-IM implant, confirming dramatic to complete fibrosis reduction along with larger muscle fiber density with crystalline GW. In contrast, controls had thick fibrosis and significant muscle atrophy, following daily muscle stimulation over 2 weeks. Scale bars=400μm. **i**) Gene expression analysis performed on bicep and gastrocnemius muscles retrieved post-stimulation indicates reduced macrophage marker-CD68, fibrosis marker-αSMactin, and inflammatory-TNFalpha for crystalline GW-coated MSDs. **j**) Quantitative analysis of muscle atrophy. All line and bar graph data:mean±SEM. Statistical analysis:one-way ANOVA plus Bonferroni multiple comparison correction *:$p<0.05$; **:$p<0.001$, and ***:$p<0.0001$; ns=not-significantly different. *In vivo*, N=5 animals/group. All subpanels reflect representative data from experimental analyses repeated 2-times for MSDs or 3-times for PDMS and CGMs.